Polarimetric Analysis of Natural Terrain Observed With a *Ku*-Band Terrestrial Radar

Simone Baffelli, *Student Member, IEEE*, Othmar Frey, *Senior Member, IEEE*, and Irena Hajnsek, *Fellow, IEEE*

***Abstract*—Terrestrial radar interferometers (TRI) are complimentary to spaceborne synthetic aperture radar systems for deformation monitoring in natural terrain: they permit shorter revisit times and greater flexibility in acquisition mode and timing. The additional diversity offered by polarimetric data can also be beneficial for TRI observations because polarized waves are sensitive to the dielectric and geometrical properties of the scatterers. Polarimetric data helps to distinguish different scattering mechanisms in a resolution cell while at the same time estimating terrain displacements. However, the polarimetric scattering signatures of natural surfaces at *Ku*-Band are not as well characterized as the ones at longer wavelengths, owing to relative rarity of full polarimetric systems operating in *Ku*-band. This band is often employed in TRI to obtain a fine azimuth resolution with a limited aperture size. This article aims at assessing the potential of polarimetric measurements in *Ku*-band TRI through an experimental study of polarimetric scattering signatures of natural surfaces using two datasets acquired over a glacier and in an agricultural and urban scene. The main finding of this analysis is that the Cloude–Pottier entropy is high for all land cover types; it is only observed to be less than 0.5 for scatterers with a large radar cross section. Several plausible hypotheses for this observation are formulated and tested, the most likely assumes a combination of depolarizing scattering from natural surfaces and the effect of the large ratio of wavelength to resolution cell size.**

***Index Terms*—Entropy, ground based radar, polarimetric radar.**

I. Introduction

A. Background

IMAGING radar systems are a fundamental tool for earth observation. Spaceborne synthetic aperture radars (SAR) are among the most widely used of these systems. These sensors provide high-resolution images of large areas regardless of solar illumination and weather conditions.

Manuscript received November 5, 2018; revised May 6, 2019 and September 9, 2019; accepted November 6, 2019. Date of publication January 14, 2020; date of current version February 4, 2020. The work of I. Hajnsek was funded by ETH Zurich. *(Corresponding author: Simone Baffelli.)*

S. Baffelli is with the Chair of Earth Observation and Remote Sensing, Institute of Environmental Engineering, ETH Zurich, 8093 Zurich, Switzerland (e-mail: bafsimon@ethz.ch).

O. Frey is with the Chair of Earth Observation and Remote Sensing, Institute of Environmental Engineering, ETH Zurich, 8093 Zurich, Switzerland, and also with the GAMMA Remote Sensing AG, 3073 Gümligen, Switzerland (e-mail: frey@gamma-rs.ch).

I. Hajnsek is with the Chair of Earth Observation and Remote Sensing, Institute of Environmental Engineering, ETH Zurich, 8093 Zurich, Switzerland, and also with the Microwaves and Radar Institute, German Aerospace Center, 82234 Wessling, Germany (e-mail: irena.hajnsek@dlr.de).

Color versions of one or more of the figures in this article are available online at http://ieeexplore.ieee.org.

Digital Object Identifier 10.1109/JSTARS.2019.2953206

A common application of these systems is differential SAR interferometry (D-InSAR): through coherent combination of images of the same scene at different times, it permits displacement estimation with a precision limited by the wavelength employed [1], [2].

By employing orthogonally polarized antennas, polarimetric imaging capabilities can be added to SAR systems [3]–[8]. The sensitivity of polarized electromagnetic waves to the geometric and dielectric properties of the objects they interact allows the separation of scattering mechanisms within a resolution cell and to characterize their scattering behavior. Example applications of polarimetric radar data are land cover classification [9], [10], the estimation of soil moisture and the reconstruction of snow and vegetation properties and structures [11]–[19].

A drawback of space—and airborne—SAR system is their high cost and the low flexibility in acquisition location and schedule. Terrestrial radar interferometers (TRI) [20], [21] are an alternative to these sensors for the observations of fast changes of limited size in natural terrain. These devices found applications in the monitoring of unstable slopes, glaciers, and subsidence in urban areas [20]–[26]. A thorough review of these systems and their application is presented in [21] and [27].

Some polarimetric TRI systems are documented in the literature; RISKSAR [25], [28]–[33] an *X*-band full polarimetric SAR mounted on a motorized rail is the most exhaustive example: the polarimetric data was employed to improve the spatial density of persistent scatterers in urban regions and to optimize the temporal interferometric phase stability for subsidence monitoring.

A rail-based system operating in *C*-band is presented in [34]; a polarimetric analysis of an urban scene acquired with it is shown in [35] and [36]. In [37] and [38], another system operating from *L*- to *X*-band is introduced, which is used in different configurations to produce polarimetric imagery and study the scattering behavior of trees and tree stands [18], [19], crops [39], and the effect of changes in soil moisture [40].

The majority of polarimetric TRI are operated at *L*-, *C*- and *X*-band, in the range of wavelengths between 30 and 3 cm. These same used by the majority of air- and spaceborne polarimetric SAR systems.

The *Ku*-band advanced polarimetric radar interferometer (KAPRI) [41] is designed for operations in *Ku*-band, at a wavelength of 17 mm. The choice of a shorter wavelength is imposed by two aspects. First, KAPRI is a real-aperture radar; this design requires a short wavelength to achieve a good azimuth resolution while keeping the antenna's size small enough for easy transportation and installation. Second, a short wavelength

1939-1404 © 2019 IEEE. Personal use is permitted, but republication/redistribution requires IEEE permission.
See http://www.ieee.org/publications_standards/publications/rights/index.html for more information.

is beneficial for zero-baseline differential interferometry as it increases the sensitivity to deformation for short repeat-time observations.

Since KAPRI uses a wavelength relatively unexplored in SAR polarimetry, an assessment of polarimetric scattering responses at this wavelength is necessary. This study aims to understand the applicability of common polarimetric scattering models to the acquisition scenarios—repeat time, geometry, resolution, and wavelength—encountered in *Ku*-band polarimetric terrestrial radar interferometry.

B. Contributions of This Article

This article presents a polarimetric analysis of two datasets acquired with KAPRI, a *Ku*-band TRA. One dataset covers the Bisgletscher glacier and the surrounding Alpine terrain, in the Southwestern Swiss Alps. The other dataset covers urban and agricultural terrain near the city of Bern.

In both datasets, high Cloude–Pottier entropy H and cross-polar backscatter power are observed over most land cover types. Four different interpretations for these observations are proposed. In the first hypothesis, the entropy is attributed to the presence of depolarizing scattering. Likely, physical mechanism for depolarization are hypothesized by relating the observed parameters with the terrain types using land cover classification data, aerial photographs, and, in the case of the polarimetric time-series dataset, with temperature measurement from a nearby automatic weather station.

Three alternative hypotheses for the high entropy, involving causes other than scattering processes are presented and tested. These hypotheses are: the effect of measurement noise, target mixing caused by spatial averaging, and mixing of the responses of several scatterers in the resolution cell.

The results of these analyses suggest that a combination of depolarizing scattering from natural surfaces, combined with the short wavelength and large resolution cell size are likely to produce the observed parameter distribution.

II. Methods and Data

A. Polarimetric Analysis

KAPRI is a coherent, fully polarimetric radar. Such radars measure the polarimetric scattering matrix $\mathbf{S}$ of every scatterer they image. The $\mathbf{S}$ matrix relates the transmitted polarization state with the polarization state of the backscattered signal. This is sufficient to describe scattering interactions with deterministic, point-like objects.

1) Depolarization: However, most natural surfaces are so-called *distributed scatterers* or *extended scatterers* that are not well modeled as point-like scatters. The response of these objects is instead modeled as the superposition of backscatter from collections of point-like scatterers with varying geometrical and electrical properties. As these elements vary in position, orientation, and properties, the total backscattered field will fluctuate in time and space and so will its polarization state. Such interactions are called *depolarizing*. The scattering matrix is insufficient to model depolarizing scattering; instead statistical descriptors are needed to quantify these interactions [42]–[44].

Since polarimetric radars only measure the fully polarized component of the backscattered signal, i.e., the scattering matrix $\mathbf{S}$, in a strict sense they cannot directly observe depolarization. To overcome this limitation, statistical descriptors for depolarizing scattering mechanism can be derived by computing the second-order statistics of $\mathbf{S}$

$$\mathbf{T} = \mathrm{E}\left[\mathbf{k}^{\intercal}\mathbf{k}\right], \mathbf{C} = \mathrm{E}\left[\mathbf{l}^{\intercal}\mathbf{l}\right] \tag{1}$$

where $\mathbf{k}$ and $\mathbf{l}$ are the Pauli and lexicographic scattering vectors, obtained as the vectorization $\mathbf{S}$ in the Pauli or lexicographic matrix basis. The average should be computed over the fluctuation of $\mathbf{S}$, which is rarely observable, especially so for imaging radar, where only one snapshot is acquired.

The common alternative is to assume *ergodicity* of the scattering process; the hypothesis that different samples of $\mathbf{S}$ acquired at different locations or times represent independent samples of the same scattering process [44].

In coherent SAR polarimetry, this is done by computing the single-look polarimetric coherence or covariance matrices $\mathbf{T}$ or $\mathbf{C}$ from $\mathbf{S}$ and averaging the result in space assuming that adjacent pixels belong to a *distributed scatterer*, i.e., a scatterer whose spatial extent is larger than a single resolution cell. This is usually assumed to hold for natural surfaces.

Several descriptors can be obtained from these matrices, which are used to model aspects of the depolarizing scattering process. In this article, the subset listed in Table I was considered.

The polarimetric backscatter coefficients have been linked to variations in environmental parameters: vegetation parameters such as water content [45], snow properties [46]–[49], soil moisture, and roughness [50]–[52] to cite some examples.

The copolar ($HH - VV$) coherence phase and magnitude are also correlated with several physical quantities, for example, the depth of fresh snow [13], the anisotropy of ice and snow particles [53], properties of snow and firn [54], and several properties of the vegetation cover [12].

$\gamma_{(HH-VV)-(HH+VV)}$ is the coherence between the $HH + VV$ and $HH - VV$ components of the Pauli scattering vector, corresponding to the normalized T_{12} element of the polarimetric coherency matrix $\mathbf{T}$. This parameter is an indicator for the presence or absence of rotational and azimuthal scattering symmetries [44]. In [11], it was shown that this coherence is correlated with the surface roughness through the extended-Bragg scattering model (X-Bragg).

Finally, the most relevant parameters considered in this analysis are the entropy H and the mean α angle of the Cloude–Pottier decomposition, obtained from the eigenvalue decomposition of the polarimetric coherence matrix $\mathbf{T}$. These are employed to describe depolarizing scattering mechanisms. The entropy H measures the amount of depolarization: a value of zero corresponds to a fully deterministic scattering process while a value of one indicates high scattering randomness. In the latter case, the coherence matrix can be expressed as the sum of three distinct polarimetric scattering matrices.

The α angle, bound between 0° and 90° is used to characterize the dominant type of scattering, with angles close to zero corresponding to single or odd-bounce scattering from point scatterers and smooth surfaces, angles around 45° anisotropic scatterers

TABLE I
SUMMARY OF THE POLARIMETRIC PARAMETERS EXTRACTED FOR THE ANALYSIS

Name	Description	Origin
Backscatter coefficients	σ^0_{HH},σ^0_{HV}, σ^0_{VH}	**C**
Normalized backscatter	polarimetric backscatter divided by the total backscatter power (span).	**C**
Copolar coherence	phase and magnitude of the complex $HH-VV$ correlation coefficient γ_{HHVV}	**C**
Cloude-Pottier decomposition parameters [43]	entropy H, mean α angle	**T**
$\gamma_{(HH-VV)-(HH+VV)}$	coherence magnitude between the first two components of the Pauli scattering vector, corresponding to the normalized T_{12} entry of the polarimetric coherency matrix.	**T**

from dipole-like objects and values close to 90° indicating even-bounce scattering from dihedral structures.

These parameters are often visualized in the H–α plane, which is used to perform a classification of observed scattering mechanism, customarily in nine zones [10], [55].

Depolarizing scattering is frequently observed in radar polarimetric observation of natural features. A literature survey shows the following three common physical mechanism behind depolarization.

1) Rayleigh scattering from a volume of anisotropic spheroidal particles with random orientations [42], [44], [56].
2) Multiple scattering in a cloud of spheroidal particles [57]–[59]. The level of depolarization increases rapidly with increasing interaction order n [44].
3) Surface scattering from a rough surface [11], [44] as predicted by the Bragg or small perturbation method (SPM) surface scattering model [60] a low frequency approximation. SPM is applicable to surfaces where the root-mean-square (rms) height s [61] is small w.r.t. the wavelength, conventionally, where $ks < 0.3$ with k being the wavenumber. At *Ku*-band, k is 367 m^{-1}, and s for agricultural soils is reported between 0.3 and 4cm [50], [62], [63]. At *Ku*-band, the X-Bragg model should be applicable to smooth soils.

However, other mechanisms not related to the scattering media are also known to increase the observed entropy [64]. Thus, the following four hypotheses ought to be considered for the analysis of polarimetric signatures.

1) the presence of depolarizing scattering mechanisms;
2) a significant noise contribution;
3) mixing of heterogeneous pixels in the multilooking process;
4) mixing of many polarized scattering processes in a resolution cell;

2) noise: Thermal noise in the radar electronics can produce observations similar to these of depolarizing scattering for non-depolarizing surfaces.

To understand how, suppose all polarimetric channels of the radar to be equally affected by noise with standard deviation σ_n. Moreover assume that the observed scatterer is not depolarizing and can be represented by a scattering matrix $\mathbf{S}$. Then, the estimated coherency matrix $\hat{\mathbf{T}}$ is

$$\hat{\mathbf{T}} = \mathbf{T} + \mathbf{I}\sigma_n^2. \tag{2}$$

Since the target is not depolarizing, $\mathbf{T}$ is a singular matrix therefore the entropy of $\mathbf{T}$ is zero. However, the estimated entropy of the observed coherency matrix $\hat{\mathbf{T}}$ is

$$H\left(\hat{\mathbf{T}}\right) = \frac{2}{\mathrm{SNR}+3}\log_3\left(\frac{1}{\mathrm{SNR}+3}\right) - \frac{\mathrm{SNR}+1}{\mathrm{SNR}+3}\log_3\left(\frac{\mathrm{SNR}+1}{\mathrm{SNR}+3}\right) \tag{3}$$

where the SNR is defined as the ratio of the nonzero eigenvalue of $\mathbf{T}$ and the noise variance σ_n^2. This function is monotonously decreasing in the SNR; the entropy will approach zero for infinite SNR. This shows that assuming *equal* noise power in all polarizations would cause an increase in estimated entropy which is not caused by depolarization in the imaged targets.

When channels are affected by different levels of noise this is not longer true. In that case, the entropy depends on the relative noise power. Therefore, if a depolarizing target is observed, a discrepancy in noise power may lower the estimated entropy by biasing one of the eigenvalues of $\hat{\mathbf{T}}$. In that case, the entropy cannot be expressed in a closed-form as a function of the noise powers since there are no formulas to compute the spectrum of sums of Hermitian matrices.

3) Mixing of Scattering Processes Due to Multilooking: Spatial averaging or *multilooking* is needed to estimate the coherency matrix $\mathbf{T}$ from the measured scattering matrix. Depending on the type of averaging, multilooking can bias entropy estimates [64], [65].

To minimize the biasing effect of multilooking adaptive, multilooking techniques are proposed [66]–[71]. These methods aim to preserve spatial resolution and avoid mixing distinct scattering mechanisms by selecting only similar pixels before averaging.

To keep higher resolution and reduce mixing, the coherency matrix can be estimated by averaging pixels in time in case time-series data is available [25], [64], [72].

Since a time series is available for one of the regions in this study, three different estimators are compared.

1) H_{boxcar}: 20×2 multilook average.
2) H_{IDAN}: Intensity-driven adaptive neighborhood (IDAN). Region growing adaptive filter [71] with a maximum region size of 40 pixels.
3) H_{temporal}: Temporal average [25], [64].

The temporal average H_{temporal} differs from the estimate discussed in [64]: in the latter, the elements of the scattering matrix are acquired in multiple passes; covariance matrices

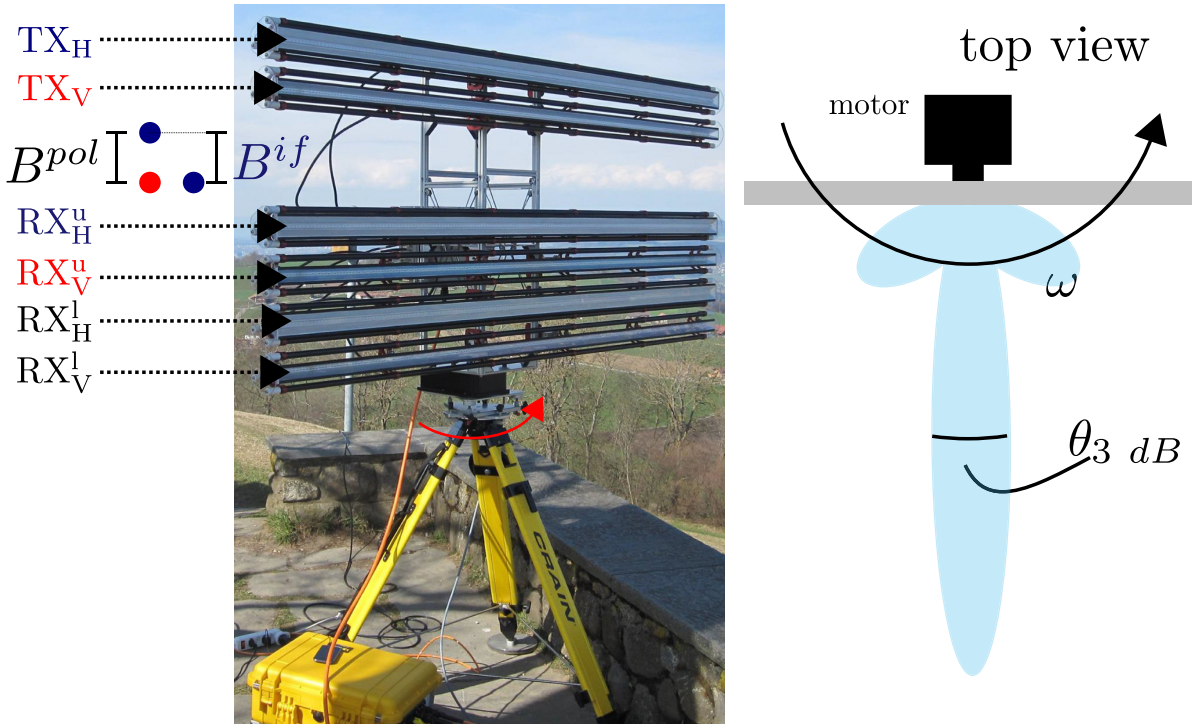

Fig. 1. Typical full-polarimetric antenna arrangement for KAPRI. The upper two antennas are the transmitters in the vertical and horizontal polarizations. Two pairs of vertical and horizontal receiving units are installed on the bottom half of the tower assembly. The two blue dots represent the locations of the equivalent phase centers for the upper and lower HH channel, and the red dot represent the phase center location for the VV channel. The tower assembly is rotated about its center with an angular velocity ω by the motor, producing 2-D images resolved by range using a frequency modulated chirp and by angle with the narrow fan beam having beamwidth $\theta_{3\,dB}$.

are then built from the stacked channels such that temporal decorrelation directly affects H_{temporal}.

For this article, all channels of $\mathbf{S}$ are acquired simultaneously and the covariance/coherence matrix are estimated from the average of single-look matrices obtained from scattering matrices measured at different times, removing the coherent effect of temporal decorrelation due to changes is the complex scattering amplitude.[1]

In order to obtain approximately the same number of looks as for the estimates obtained from spatial averages, 40 acquisitions are used to estimate H_{temporal}. These are chosen to be as close as possible in time, to minimize the effect of changes in the scene.

B. Mixing Within a Resolution Cell

The combination of many scatterers due to a large resolution cell size may also cause high entropy to be estimated.

The level of entropy is affected by the number and types of targets contained a resolution cell. If a cell comprises a low entropy scatterer with a large radar cross section such as a trihedral reflector, the entropy will be low. Otherwise, if the cell contains several scatterers of similar radar reflectivity but differing shape and orientation, the entropy will be higher. Since its estimation requires averaging, if neighboring cells also contains a mixture of targets with similar properties, the spatial estimate of entropy will be high.

[1]Although not its indirect effect due to changes in the imaged scene that may increase the entropy.

This effect is controlled by the wavelength. Substantial scattering comes from objects larger than several wavelengths. Therefore, as the ratio of wavelength to resolution cell size decreases, the entropy will increase as the number of scatterers per resolution cell is expected to increase, which will in turn increase the entropy.

C. Data Acquisition: KAPRI

KAPRI [41] is a *Ku*-band polarimetric real aperture radar developed from Gamma portable radar interferometer II (GPRI-II) [73]. GPRI-II initial application is slope instability monitoring using differential interferometry. While the GPRI-II employs vertically polarized antennas, KAPRI was upgraded by the manufacturer through the addition of a set of horizontally polarized antennas and switching circuitry in order to acquire fully polarimetric datasets.

KAPRI operates at 17.2 GHz, corresponding to a wavelength of 0.017 m. Distance resolution is obtained using a 200 MHz chirp, processed with the deramp-on-receive frequency modulated continuous wave (FMCW) architecture [74]. The chirp produces a nominal range resolution of 0.75 m, which increases to an effective resolution of approximately one meter after range windowing, necessary for sidelobe suppression based on the fast Fourier transform (FFT) range compression.

Resolution orthogonal to the line of sight is obtained by scanning a 2 m-long slotted waveguide antenna having a beamwidth of 0.385° with an azimuthal drive. The principle is illustrated

TABLE II
MOST IMPORTANT HARDWARE PARAMETERS OF KAPRI

Parameter	Value
Modulation	FMCW ($250\,\mu$s to 16 ms chirp duration)
Center frequency	17.2 GHz
Bandwidth	200 MHz
Range resolution	0.95 m 3 dB resolution -26 dB peak sidelobe ratio (PSLR)
Azimuth 3 dB beamwidth	0.385°
Elevation 3 dB beamwidth	35°
Polarization	fully polarimetric, selectable TX and RX polarization
Polarimetric Isolation	better than 30 dB
Residual copolar phase imbalance	less than 10°

in Fig. 1. With this method images are acquired on a polar grid, with trapezoidal resolution cells whose cross-range size increases linearly with distance from the radar: the ground resolution in cross range is 8 m at a distance of 1 Km.

The hardware characteristics of KAPRI are summarized in Table II.

D. Data Preparation and Calibration

For a valid polarimetric analysis it is necessary that radar data is processed and calibrated correctly. The methods employed for this purpose are described in detail in another publication [41]. The following paragraphs provide a short overview of the procedure for the benefit of the reader.

KAPRI is based on a dechirp-on-receive FMCW architecture, where the system transmits a chirped continuous wave signal; the backscatter signal received by the antenna is then mixed with the transmitted chirp, producing a modulated signal whose beat frequency is proportional to range. This beat signal is digitized and range profiles are reconstructed using a Fourier transform [41], [75].

To obtain two-dimensional (2-D) images, a series of range profiles at different antenna azimuth angles are acquired, resolving the scatterers by their range and by their angle thanks to a narrow fan beam emitted by a slotted waveguide antenna, as illustrated in Fig. 1. However, during the chirped the relative phasing of the radiation emitted at the antenna's slot change, causing an antenna mainlobe squint [76] leading to the degradation of range and azimuth resolution.

To correct this effect, the raw data matrix acquired in the chirp frequency–azimuth angle domain—often called fast time and slow time, respectively—is processed with a frequency–azimuth interpolation to align the samples along in the correct angle–frequency bins. After squint compensation and range compression the SLC data must be corrected with an azimuth matched filter to remove the azimuth phase ramp caused by the eccentric motion of the antenna's phase centers as the antenna are mounted offset from the motor's center of rotation. This correction is done according to the procedure detailed in a previous publication [41].

The polarimetric channels are coregistered by interpolation using the HH channel as a reference with the purpose of correcting a 0.18° antenna mainlobe pointing difference between the horizontally and the vertically polarized antennas. The pattern misalignment reduces the signal-to-noise (SNR) ratio for HV channel by 1.8 dB with respect to the SNR for the copolar channels because the transmission and reception patterns do not completely overlap.

KAPRI uses separate transmitting and receiving antennas for the H and the V polarizations to minimize crosstalk. The antennas are installed with vertical spacing on a metal truss, which is on turn attached to the azimuth drive motor, as shown in Fig. 1. Because of the spatial separation of the equivalent polarimetric antenna phase centers—as shown by the diagram in Fig. 1 where the equivalent phase center locations for the HH and VV for the upper receiver are displayed as blue and red dots respectively—the entries of scattering matrix $\mathbf{S}$ have a different propagation phase.

Therefore, phase differences computed from channels where the phase centers are not at the same height will contain a phase term proportional to the terrain topography and to the baseline. A method to remove this contribution from a single look polarimetric covariance matrix $\mathbf{C}$ was presented in [41]. The method was latter modified to operate on scattering matrices: the absolute topographic phase is estimated using two channels with the same polarization located at two ends of a baseline; then unwrapped, rescaled to the baseline between each channel's phase center and the reference phase center placed at the location of the top transmitting antenna and subtracted from the channel's phase.

After removal of the topographic phase, the polarimetric and radiometric calibration parameters determined using the dataset and procedure described in [41] are applied to $\mathbf{S}$.

Finally, radiometric normalization is applied by dividing the entries of the scattering matrix $\mathbf{S}$ with the pixel area factor, determined using an external digital elevation model geocoded in radar azimuth-range coordinates [77], [78]. This generates a scattering matrix where the pixel's intensities correspond to the equivalent normalized radar crossection σ^0.

E. Datasets

The polarimetric analysis presented in this article is made with two datasets acquired in 2015 and 2016 in two regions of Switzerland.

The first data was taken in the summer months of 2015 during a glacier monitoring project in the Mattertal, an Alpine valley in the Southwestern Swiss Alps, Canton of Valais.

The second dataset was acquired in September 2016 during a calibration experiment at the "Chutzen" location, at the top

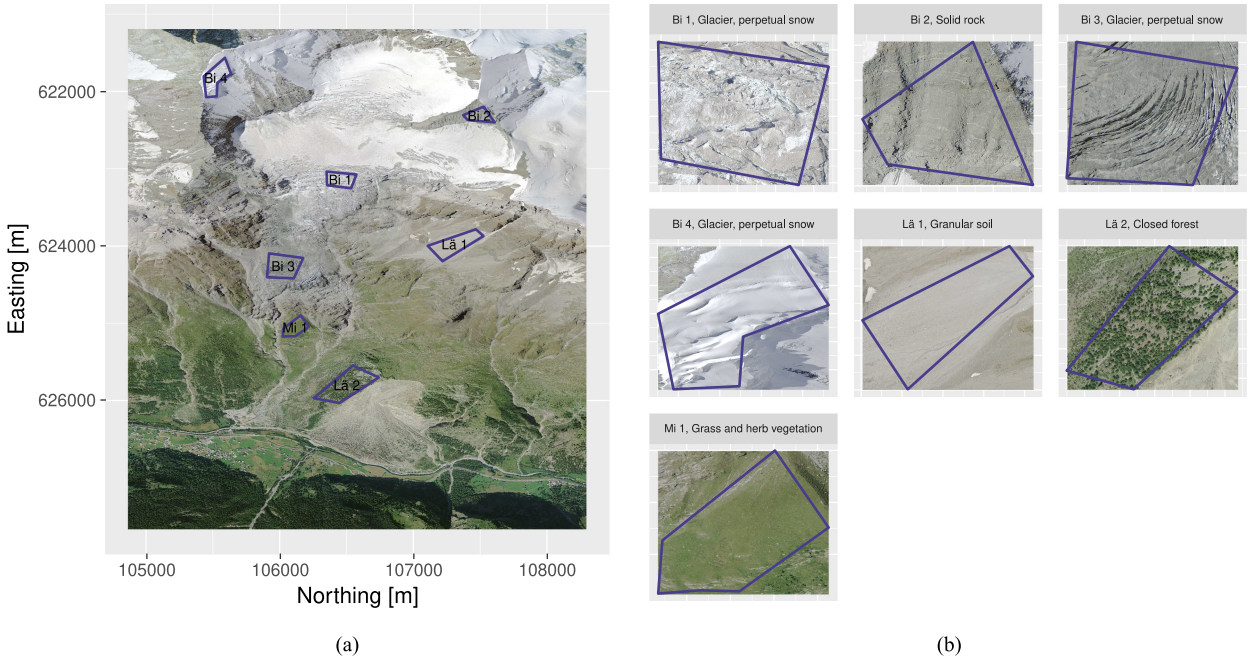

Fig. 2. (a) 0.25 m resolution orthophoto of the Bisgletscher test site. The ROIs used for the polarimetric analysis are overlaid to the image in dark blue and are assigned a short alphanumeric code. (b) Zoom-ins of each ROI, including its full name according to the *SWISSNAMES* placename inventory and the land cover class from the NOLC04 land use statistics. The alphanumeric codes in three correspond to the first two character of the ROI's name followed by an increasing number. (Geodata ©swisstopo). (a) Overview map for Bisgletscher. (b) Excerpts for Bisgletscher ROIs.

of the "Belpberg" hill, near the town of Münsingen, Canton of Bern, Switzerland.

1) Bisgletscher Dataset: The data was acquired during a project to monitor the surface ice flow velocity of the Bisgletscher [79] glacier in the Mattertal valley, Canton of Valais, Southwestern Swiss Alps. The device was installed in the vicinity of the Domütte alpine hut, where electrical power supply and a Wi-Fi communication and control link used by the PermaSense/X-Sense project [80] were available. From its location at the hut, KAPRI was overlooking the Bisgletscher on the other flank of the valley at distances between 3000 and 8000 m, where the terrain is covered by glaciers, rocks, scree, short vegetation, and sparse forests. An overview of the scene is given by the aerial photograph of Fig. 2(a).

The campaign was carried out in the summer months of 2015, between the second half of July and September, using acquisition repeat times of 150 s. Because of data transmission and storage limitations, acquisition were only made for 12 h each day.

Only a subset of the whole time series could be analyzed as processing the entire dataset would have exceeded the available storage and computation capabilities. The analysis is focused on the week between July 10 and July 17, 2015. Ten acquisition times were used for each of these days: 6:00, 7:00, 8:00, 9:00, 10:00, 12:00, 14:00, 15:00, 16:00, and 18:00 Coordinated Universal Time. The local time is Central European Summer Time.

An averaging window of 20 pixels in range and 2 in azimuth is used to estimate the polarimetric covariance matrices used to extract polarimetric parameters. The choice of a rectangular window with a high aspect ratio is imposed by the polar acquisition geometry. If too many azimuth pixels are used in the averaging, the angular resolution is greatly degraded and pixels representing widely different targets on the ground would have been averaged together; however, enough samples are necessary for a robust estimate of the second-order statistics. Since the range resolution is finer than the azimuth resolution, a larger averaging factor in range gives approximately square pixel in the middle of the scene: namely 20 m $\times$ 50 m at a slant range of 6000 m.

2) Chutzen Dataset: The scene covers slant range distances between 50 m and 3 km. An aerial photograph of the scene is shown in Fig. 3(a).

This measurement was acquired during a calibration and validation campaign; to this end, five trihedral corner reflectors—of which three have triangular faces with 40 cm side length and two have cubic faces with the same size—were placed at distances between 70 m and 3 km from the radar. More details on the acquisition campaign and the polarimetric calibration are found in [41].

Data processing is automated with Nextflow [81], a scientific workflow management system, to ensure consistent and reproducible analyses.

For each dataset a number of polygonal region of interest (ROIs) are selected over the extent of the data, each representing different terrain features. These ROIs are drawn in a geographical information system on a 0.25 m orthophoto [82] of the investigated area, ensuring that each polygon only consist of one land cover type. Then, the land cover type according to the NOLC04 [83] land cover inventory is added to the polygons and each ROI is assigned a name taken from the nearest feature in the *SWISSNAMES* geographic name inventory provided by

Fig. 3. The geographic situation of the Chutzen dataset. (a) Overview of the area using a 0.25 m resolution orthophoto. (b) Zoomed-in photographs corresponding to the ROIs used for the polarimetric analysis. The title of each panel gives the ROI's land cover type according to the NOLC04 land cover survey and its name according to the *SWISSNAMES* Swiss placename inventory (Geodata ©swisstopo). (a) Overview map for Chutzen. (b) Excerpts for Chutzen ROIs.

Swisstopo [84]. Finally, these polygons are converted to range-azimuth coordinates using a geocoding lookup table generated with an external DEM (SWISSALTI3D by Swisstopo) with a posting of 2 m [85].

The shape of the ROIs is shown in the map of Fig. 3(a) where they are assigned a short alphanumeric code; detailed excerpts of the aerial photograph showing individual ROIs with their land cover class and name are displayed in Fig. 3(b).

III. Results

The results of the polarimetric analysis are described for each dataset. First, the variability of the parameters within the ROIs, between land cover types and—in the case of the Bisgletscher time series—are addressed.

This is followed by an analysis of parameter maps, to assess the presence of large-scale spatial patterns.

Finally, entropy maps obtained with the three different estimators explained in Section II-A1 are shown for the Bisgletscher dataset.

A. Bisgletscher

1) ROI-By-ROI Analysis: A visual representation of the variability of the selected parameters in time and within the ROIs is made by plotting them as a time series in Figs. 4 and 5. Dots are used to mark the average of each ROI at any time, vertical bar show $\pm$ 1 standard deviations from the mean. The solid line is a GAM-smoothed estimated, superimposed to the plot to facilitate the detection of temporal trends.

Each panel of the plot shows the time series for an individual ROI, with the title giving the code corresponding to the codes shown in Fig. 2(a); These short codes are derived from the first three characters of the name shown in each panel of Fig. 2(b) and a number.

A quantitative summary of this information, as a table of mean and standard deviation values for each ROI, is displayed in Table III. Table IV shows the standard deviation of the parameter computed along the time series.

In the following sections, the most salient observations made in each ROI will be highlighted to facilitate later interpretation.

1) "Bi 1": Entropy and α decrease in time. Copolar coherence magnitude increases. Backscatter is initially dominated by the crosspolarized signal, increase of copolar backscatter after July 12.
2) "Bi 2": High entropy, all parameters are stable in time except for daily variations in backscatter power and an increase of copolar coherence on July 18. Backscatter is primarily crosspolarized.
3) "Bi 3": High entropy. Backscatter predominantly crosspolarized, showing diurnal variations.
4) "Bi 4": High entropy, decreases on July 12, regular diurnal variations. Backscatter predominantly crosspolarized, again showing diurnal variations and overall decreasing.
5) "Lä 1": High entropy, all parameters stable in time except for an increase in copolar coherence on July 18. Backscatter crosspolarized, showing a drop on July 18.
6) "Lä 2": High entropy, low Pauli coherence, parameters do not significantly vary in time. Backscatter is predominantly crosspolarized, ratio decreases on July 18.

2) Spatial Distribution of Parameters: The results of the polarimetric analysis show that the parameters do not considerably

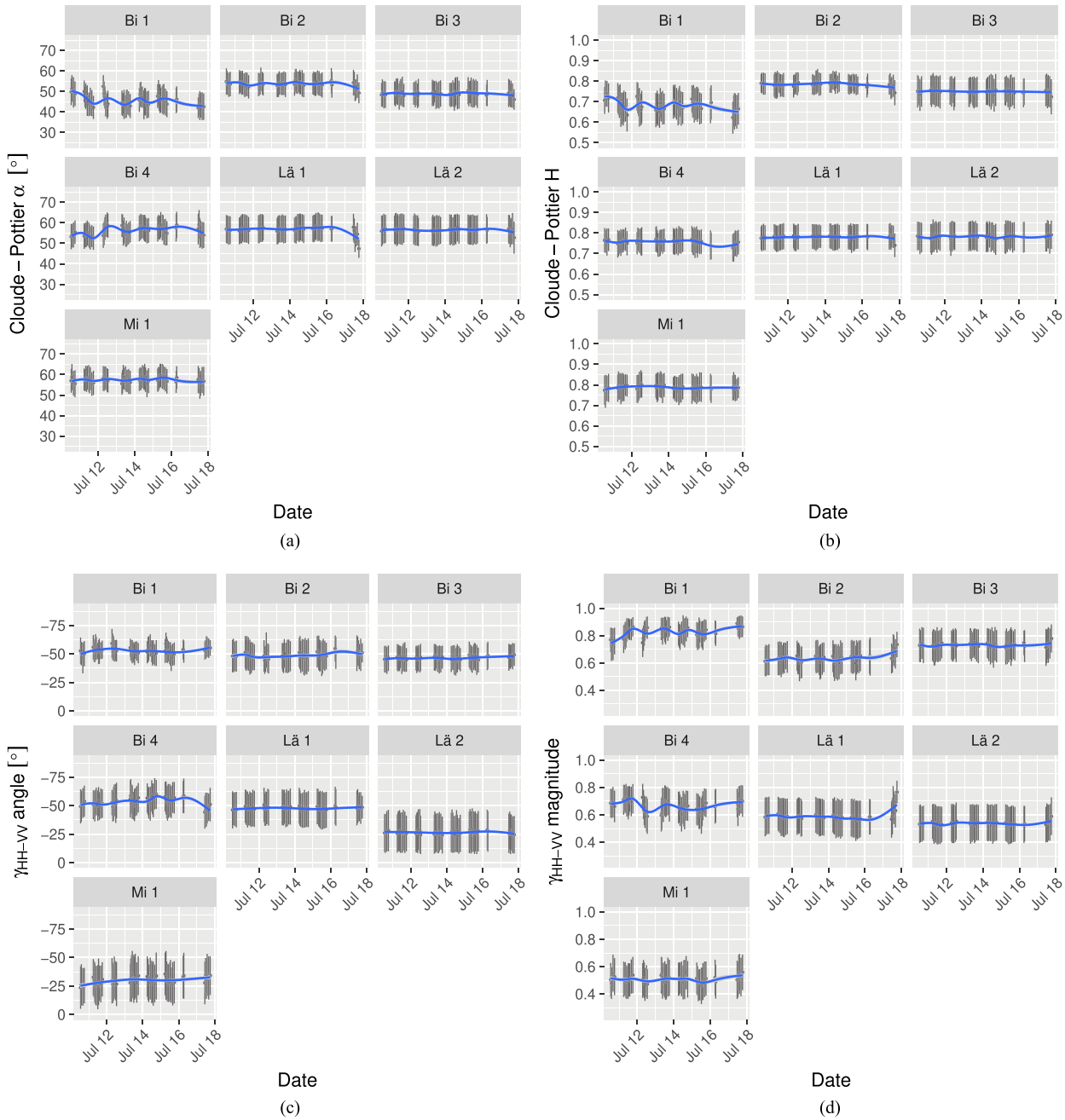

Fig. 4. Temporal and spatial variability of (a) mean α, (b) Cloude–Pottier entropy H, (c) copolar phase difference, and (d) copolar coherence for the ROIs in the Bisgletscher scene shown in Fig. 2. The vertical lines display +/-1 standard deviation for data within each ROI, computed over all the pixels the blue line shows a smoothed trendline obtained with ggplots "GAM" smoother.

vary over time for most of the ROIs. Therefore, by selecting one date and plotting the parameter map, their large-scale behavior over the entire scene can be assessed.

These plots should help to assess whether the selected ROIs are representative and if there are spatial trends at larger scales. The plot are derived from a dataset taken on July 14.

In the entropy map [see Fig. 6(a)] the difference between areas located in radar shadow and the rest of the scene is visible; the locations of shadow are seen in the Pauli RGB composite in Fig. 6(c) as the dark areas in the upper part of the image.

Except for this no other trends are observed. The entropy is between 0.6 and 1.0 over the entire scene. A region of lower entropy is visible in the center of the scene; this part corresponds to the glacier, which appears dark blue in the Pauli RGB composite.

The entropy estimated using temporal averaging [see Fig. 7(b)] shows a different behavior and a larger spatial variability. Its value is lower than the spatial estimate, particularly in correspondence of rock faces as "Bi 2" and left and right of the glacier. The IDAN estimate on the other hand shows little difference from the spatial multilook estimate.

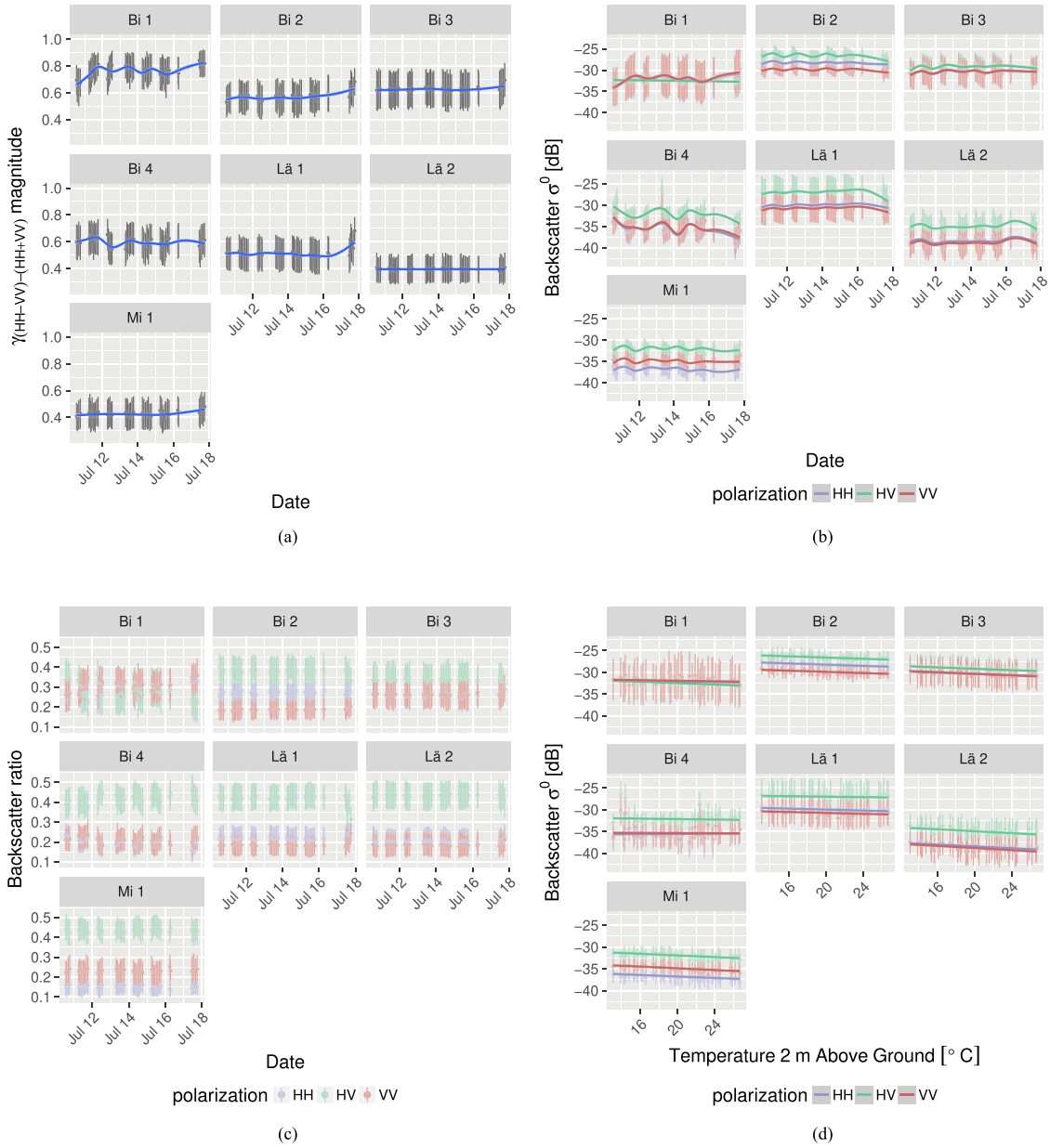

Fig. 5. Temporal and spatial variability of parameters in the ROIs of the Bisgletscher data. The panels show (a) magnitude of $\gamma_{(HH-VV)-(HH+VV)}$, (b) backscatter in decibel, (c) normalized backscatter, and (d) backscatter versus air temperature measured at the "Zermatt" weather station. The vertical lines around each point display $+/-1$ standard deviation, computed over all the pixels in that ROI. The red, blue, and green lines in the backscatter plots encode the polarization (VV, VV, HV). (a) $\gamma_{(HH-VV)-(HH+VV)}$: coherence magnitude between the first two components of the Pauli scattering vector, Bisgletscher dataset. (b) Spatio-temporal variability of backscatter in dB. (c) Spatio-temporal variability of normalized backscatter. (d) Backscatter against air temperature, as measured by the "Zermatt" Automatic Weather Station.

TABLE III
MEAN AND STANDARD DEVIATION OF THE POLARIMETRIC PARAMETERS FOR THE BISGLETSCHER SCENE, GROUPED BY ROI

Name	Incidence[°]	HH [dB]	HV [dB]	VV [dB]	H	α	$\angle HHVV$ [°]	γ_{HHVV}
Bi 1	60.1	-29.65 (-28.4)	-31.24 (-32.2)	-29.57 (-28.5)	0.66 ($1.2 \cdot 10^{-1}$)	45.66 (6.7)	-52.81 (10.3)	0.82 ($9.5 \cdot 10^{-2}$)
Bi 2	49.7	-27.98 (-32.5)	-26.32 (-30.6)	-29.69 (-34.5)	0.79 ($5.2 \cdot 10^{-2}$)	53.67 (5.7)	-48.7 (15.1)	0.63 ($1.3 \cdot 10^{-1}$)
Bi 3	66.8	-29.21 (-30.2)	-28.44 (-30.5)	-29.18 (-30.2)	0.75 ($7.8 \cdot 10^{-2}$)	48.87 (6.3)	-46.35 (11.5)	0.73 ($1.2 \cdot 10^{-1}$)
Bi 4	67.9	-34.34 (-35)	-31.29 (-31.9)	-34.18 (-34.6)	0.75 ($6.6 \cdot 10^{-2}$)	56.16 (6.7)	-53.44 (16.2)	0.66 ($1.3 \cdot 10^{-1}$)
Lä 1	73.5	-29.09 (-31.7)	-25.78 (-27.3)	-29.82 (-32)	0.78 ($6.2 \cdot 10^{-2}$)	56.74 (6.8)	-47.69 (17.6)	0.58 ($1.5 \cdot 10^{-1}$)
Lä 2	55.7	-37.57 (-39.2)	-33.87 (-34.4)	-37.79 (-38.9)	0.78 ($7.2 \cdot 10^{-2}$)	56.52 (7.3)	-17.72 (28.6)	0.51 ($1.6 \cdot 10^{-1}$)
Mi 1	57.9	-36.39 (-39.6)	-31.63 (-35.4)	-34.57 (-38.3)	0.79 ($6.5 \cdot 10^{-2}$)	57.52 (6.1)	-22.36 (26.8)	0.48 ($1.5 \cdot 10^{-1}$)

The statistics are computed over time and space.

TABLE IV
TEMPORAL STANDARD DEVIATION OF THE POLARIMETRIC PARAMETERS FOR THE BISGLETSCHER SCENE, GROUPED BY ROI

Name	HH [dB]	HV [dB]	VV [dB]	H	α	γ_{HHVV}	$\angle HHVV$ [°]
Bi 1	-29.9	-32.9	-30	$6.3 \cdot 10^{-2}$	3.8	$4.8 \cdot 10^{-2}$	4
Bi 2	-33.2	-31.9	-35.4	$3.1 \cdot 10^{-2}$	4.5	$1 \cdot 10^{-1}$	10.7
Bi 3	-30.7	-31.4	-30.8	$4.9 \cdot 10^{-2}$	3.9	$7.3 \cdot 10^{-2}$	3
Bi 4	-37.3	-35.2	-36.9	$3.2 \cdot 10^{-2}$	3.8	$6.1 \cdot 10^{-2}$	4.9
Lä 1	-32	-27.6	-32.2	$4.7 \cdot 10^{-2}$	5.7	$1.3 \cdot 10^{-1}$	13.6
Lä 2	-39.6	-34.8	-39.3	$3.6 \cdot 10^{-2}$	5	$9.9 \cdot 10^{-2}$	14.8
Mi 1	-40.3	-36.7	-39.3	$3.3 \cdot 10^{-2}$	3.3	$8.8 \cdot 10^{-2}$	14.2

The standard deviation is computed on the mean of the parameter, which are aggregated by ROI.

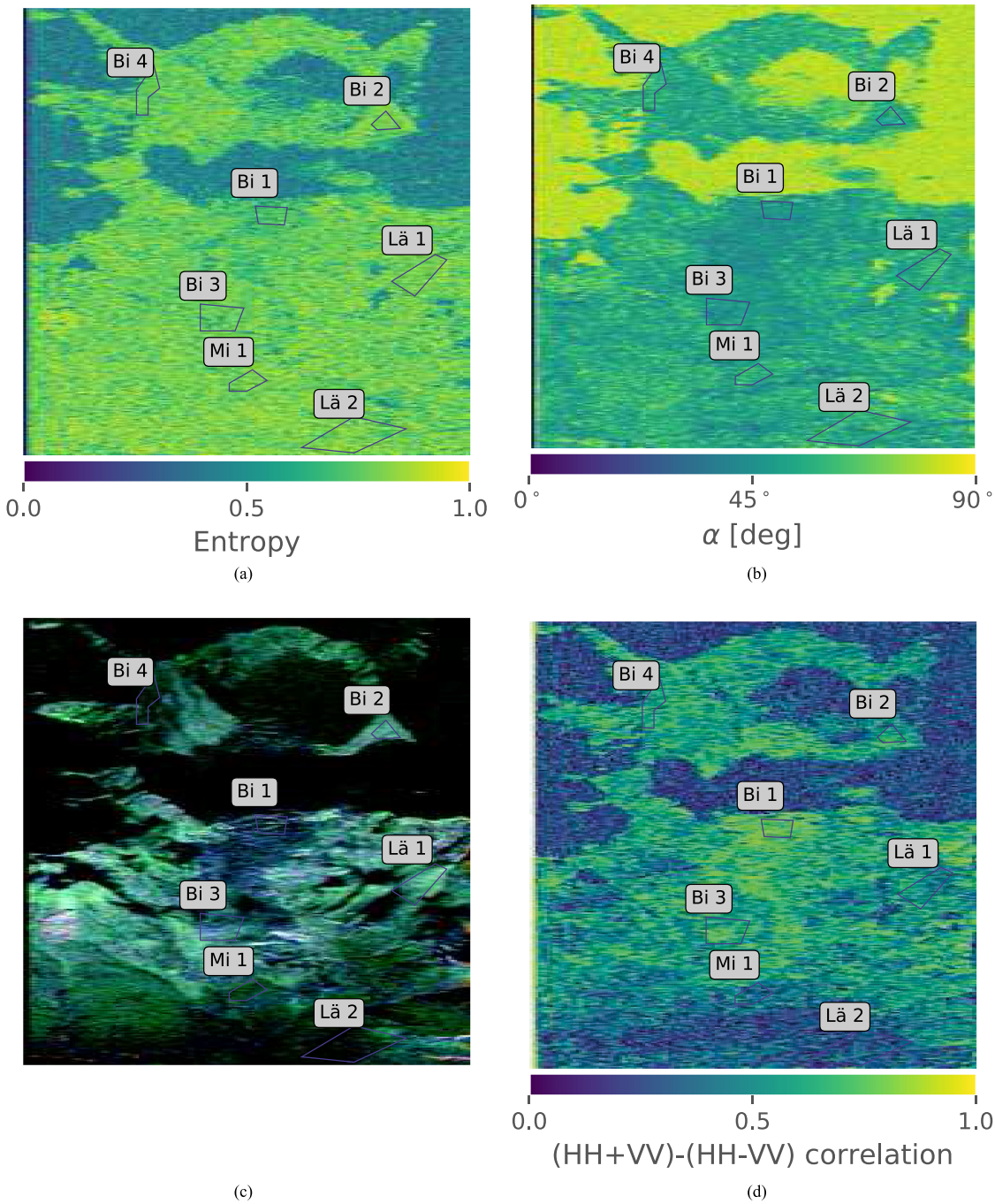

Fig. 6. (a) Cloude–Pottier entropy H, (b) mean α, (c) Pauli RGB composite, and (d) magnitude of $\gamma_{(HH-VV)-(HH+VV)}$ for the Bisgletscher dataset. The parameters were estimated with a 20×2 boxcar filter.

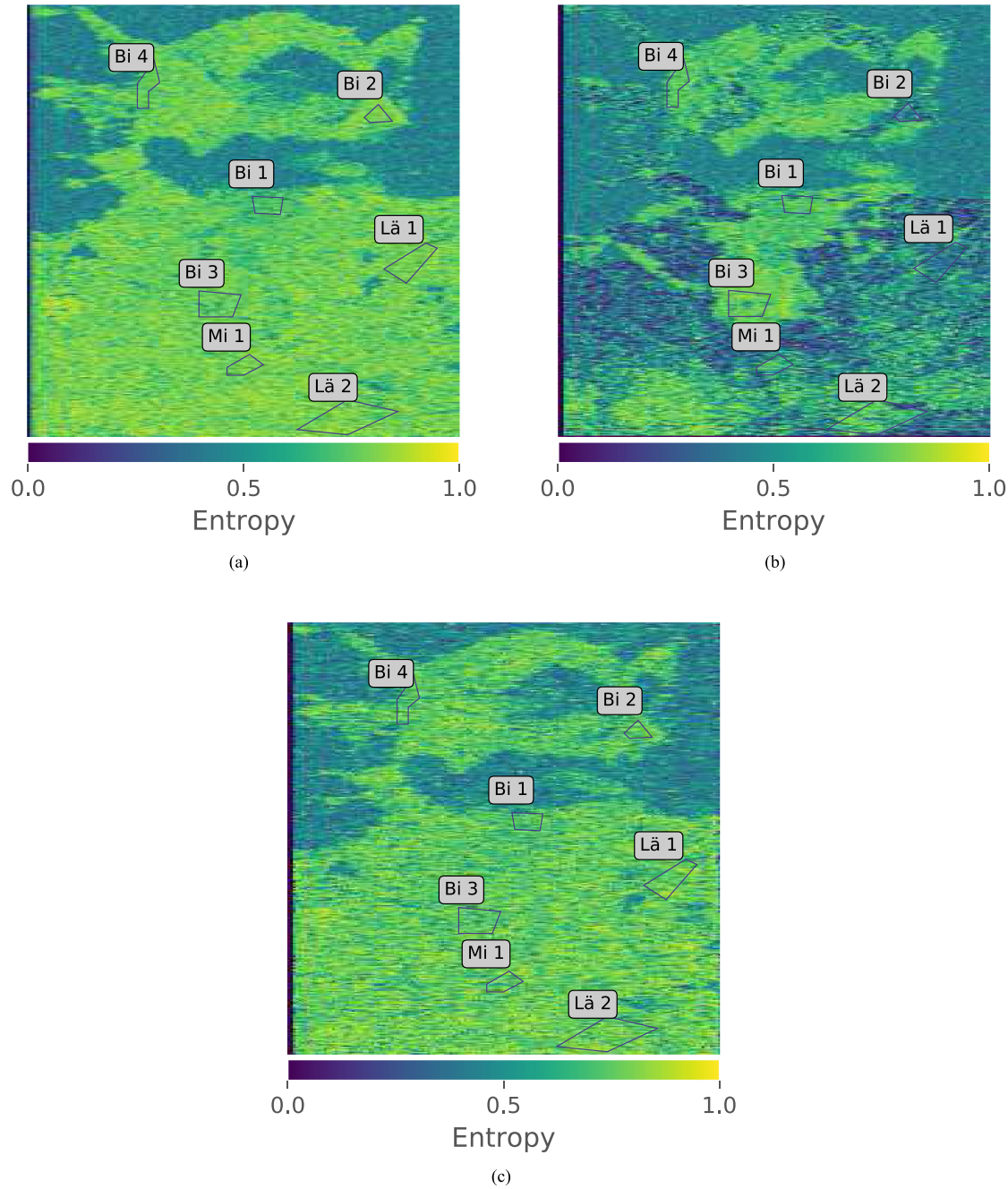

Fig. 7. (a) Comparison between the entropy estimated by spatial averaging. (b) Estimate made using temporal averaging. (c) Estimate obtained using the IDAN filter. (a) H_{boxcar}: Cloude-Pottier entropy estimated by spatial averaging. (b) $H_{temporal}$: Cloude-Pottier entropy estimated by temporal averaging. (c) H_{IDAN}: Cloude-Pottier entropy estimated with spatial averaging using the IDAN region-growing filter.

The α angle is high throughout the image and only shows an area of lower values in the center, in correspondence with the glacier. Except for the radar shadow, no areas where α is higher than 60° are observed.

Outside of the glacier, where surface scattering appears dominant (blue–violet in the Pauli RGB composite), HV backscatter (green color in the Pauli RGB) is predominant, as observed in the time-series plot presented in Section III-A1.

The highest values of $\gamma_{(HH-VV)-(HH+VV)}$ are observed in correspondence of the glacier [see Fig. 6(d)] in the middle of the scene; they correspond to blue areas in the the Pauli RGB composite and where the entropy and α show the lowest values.

B. Chutzen

1) ROI-By-ROI Analysis: Since no time series is available for the Chutzen dataset, the ROI-wise analysis will be performed on 2-D histograms of the Cloude–Pottier parameters and on histograms of the polarimetric backscatter, of the copolar

TABLE V
MEAN AND STANDARD DEVIATION OF THE POLARIMETRIC PARAMETERS FOR THE CHUTZEN SCENE, GROUPED BY ROI

Name	Incidence[°]	HH [dB]	HV [dB]	VV [dB]	H	α	$\angle HHVV$ [°]	γ_{HHVV}
Er 1	81.8	−24.82 (−20)	−26.07 (−21)	−25.79 (−21.3)	$0.65\ (1.8 \cdot 10^{-1})$	51.59 (14.7)	−4.28 (83.8)	$0.54\ (2.2 \cdot 10^{-1})$
Go 1	81	−41.08 (−45.2)	−39.76 (−44.9)	−40.13 (−44.4)	$0.75\ (5.3 \cdot 10^{-2})$	44.19 (7.5)	2.86 (12.5)	$0.73\ (9.7 \cdot 10^{-2})$
Hi 1	80	−40.63 (−43.4)	−37.22 (−40.5)	−40.05 (−43.6)	$0.76\ (6 \cdot 10^{-2})$	52.49 (6.6)	−10.74 (19.8)	$0.63\ (1.3 \cdot 10^{-1})$
Mo 1	82.4	−38.97 (−43.4)	−40.01 (−44.8)	−38.75 (−43.1)	$0.64\ (9.8 \cdot 10^{-2})$	34.55 (8.8)	−3.99 (9)	$0.84\ (1.1 \cdot 10^{-1})$
Mü 1	80.5	−24.08 (−19.9)	−31.35 (−29.7)	−24.59 (−20.3)	$0.58\ (2 \cdot 10^{-1})$	37.06 (13.6)	−4.96 (35.2)	$0.71\ (2 \cdot 10^{-1})$
Ut 1	80	−44.39 (−42)	−39.01 (−38.4)	−43.28 (−41.6)	$0.68\ (1 \cdot 10^{-1})$	62.12 (7.6)	1.55 (33.7)	$0.5\ (1.8 \cdot 10^{-1})$

The statistics are computed over all pixels in each ROI.

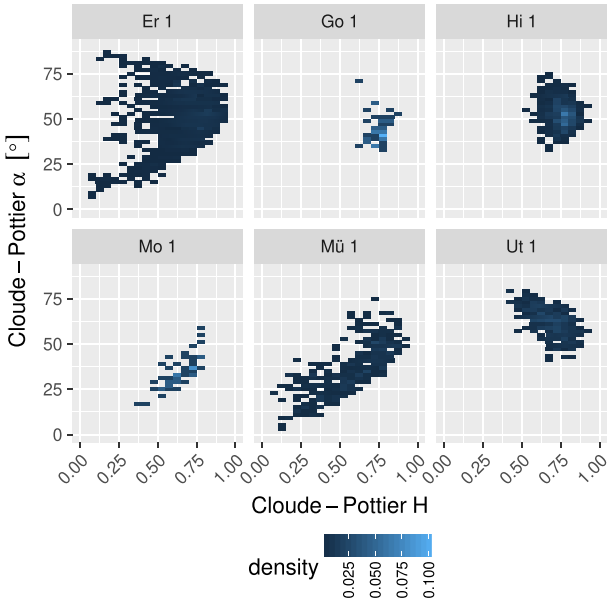

Fig. 8. Cloude–Pottier H-α histogram for the Chutzen dataset. The title of each panel corresponds to the ROI's name, as shown in Fig. 3(b).

coherence and $\gamma_{(HH-VV)-(HH+VV)}$. A summary of the polarimetric parameters is shown in Table V.

The H-α histogram grouped by ROI are shown in Fig. 8, the histograms of the polarimetric backscatter in Fig. 9(a), the histogram of $\gamma_{(HH-VV)-(HH+VV)}$ in Fig. 9(d), and those of the copolar coherence magnitude and phase in Fig. 9(b) and (c).

1) "Er 1": Large variance in α, entropy, backscatter, and polarimetric coherence. Backscatter distribution equal in all channels
2) "Go 1": Very concentrated in Cloude–Pottier diagram, low variance in all parameters. Backscatter levels similar in all channels. High entropy, α, and $\gamma_{(HH-VV)-(HH+VV)}$.
3) "Hi 1": Parameter distribution concentrated in Cloude–Pottier histogram. Backscatter predominantly HV, high entropy.
4) "Mo 1": Cloude–Pottier parameters concentrated. Backscatter predominantly copolarized. Medium entropy, α lower than other ROIS. Highest copolar coherence of all ROIS.
5) "Mü 1": Low entropy and α, zero copolar phase difference and predominantly copolar backscatter. High $\gamma_{(HH-VV)-(HH+VV)}$.
6) "Ut 1": High α, low copolar phase difference with larger variance.

2) Spatial Distribution of Parameters: The entropy map is shown in Fig. 10(a); its average value is lower than in the Bisgletscher scene. It also shows a larger spatial variability. Several low-entropy points can be observed in "Mü 1" and "Erl 1" as well to the immediate top right of "Hi 1."

The mean α angle is lower, at $45°$, as seen in Fig. 10(b). Pixels with much lower α are seen, corresponding to the pixels of low entropy observed previously. Likewise, pixels with α close to $90°$ are observed, again in correspondence to low-entropy pixels. All these points match with very bright features in the Pauli RGB composite. On the aerial photograph, most of these points correspond to individual buildings.

The map of $\gamma_{(HH-VV)-(HH+VV)}$ is displayed in Fig. 10(d); correlation with entropy is visible. Points of low entropy appear to have a very high coherence value, while in the rest of the scene the coherence is low.

IV. DISCUSSION

The most salient result of the polarimetric analysis is the high entropy, as displayed by the Bisgletscher entropy map in Figs. 6(a) and in 10(a) for Chutzen. In the latter case, entropy is observed to be lower than 0.5 for individual buildings of large scattering cross section in urban areas.

For the Bisgletscher scene, the α angle is no lower than $45°$ for any of the ROIs. None of the parameters show large temporal variation [see Fig. 4(a) and (b)].

A large fraction of crosspolarized backscatter is observed for most ROIs (see Fig. 5 for Bisgletscher), the histogram in Fig. 9(a) for Chutzen—and Tables III and V.

This combination of high entropy and crosspolarized backscatter hints at the presence of depolarizing scattering mechanism [44].

This is realistic considering the dominant land cover types encountered in both areas—ice, gravel, and vegetation—whose scattering behavior at *Ku*-band is presumably well-approximated by random media.

1) Bisgletscher: In the following list, the time-series plots shown in Section III-A1 will be interpreted ROI-by-ROI with the help of the orthophotos of Fig. 2(b) and the land cover classification data, linking the observations to land cover types and changes in environmental parameters, linking them to the depolarizing scattering mechanisms discussed in Section II-A1.

1) "Bi 1" is classified as glacier in the land cover map; it is located in the middle of the lower icefall of Bisgletscher.

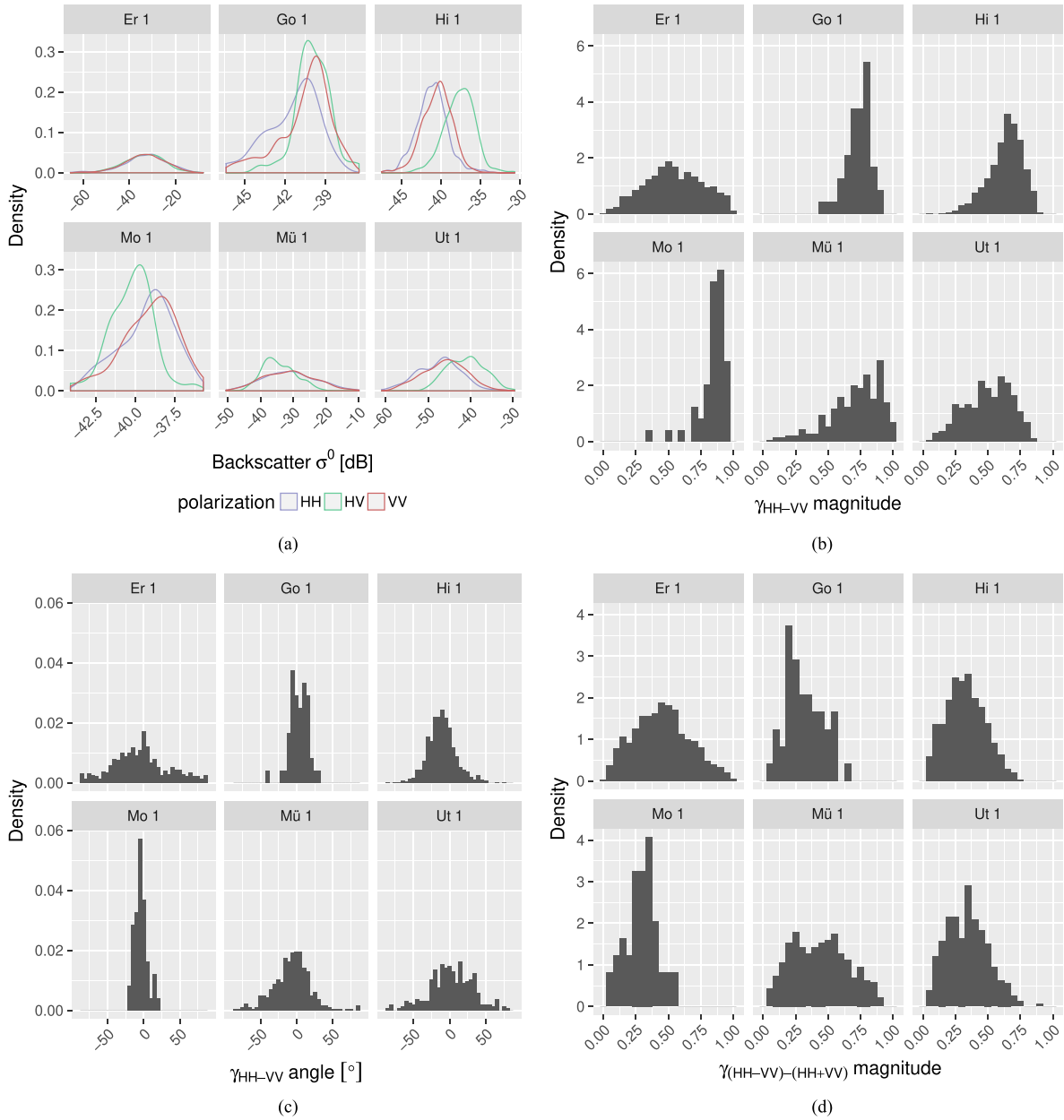

Fig. 9. Histograms of (a) polarimetric backscatter coefficient, (b) copolar coherence magnitude, (c) copolar coherence phase, and (d) coherence magnitude of $\gamma_{(HH-VV)-(HH+VV)}$. The title of each panel indicates the short code of each ROI plotted in Fig. 3(b).

The observed Cloude–Pottier corresponds to mechanisms between *Zone 5: Medium Entropy Vegetation Scattering* and *Zone 4: Medium Entropy Multiple Scattering* of the Cloude–Pottier classification scheme.

This value of α is typical of anisotropic, dipole-like scatterers such as needles and branches. The high entropy is related to a broad distribution of the scatterer's orientation angles. As the penetration depth of *Ku*-band electromagnetic radiation in wet ice—as it can be encountered on a glacier's surface in summer—is almost zero,[2] volume scattering from anisotropic ice crystals is unlikely under these conditions. The high copolar coherence magnitude is also evidence for the lack of volumetric scattering, since polarimetric coherencies for a random volume should be $1/3$ according to theory [89].

Medium entropy surface scattering seems likely given the high copolar coherence magnitude and low copolar phase dispersion, and the low level of crosspolarized backscatter and the similar magnitude of the HH and VV backscatter coefficients. The temporal increase in $\gamma_{(HH-VV)-(HH+VV)}$ and the drop of H and crosspolar scattering power are presumably related to decreasing surface roughness [11].

[2]Nonetheless, far greater penetration is observed in cold and dry ice [86]–[88].

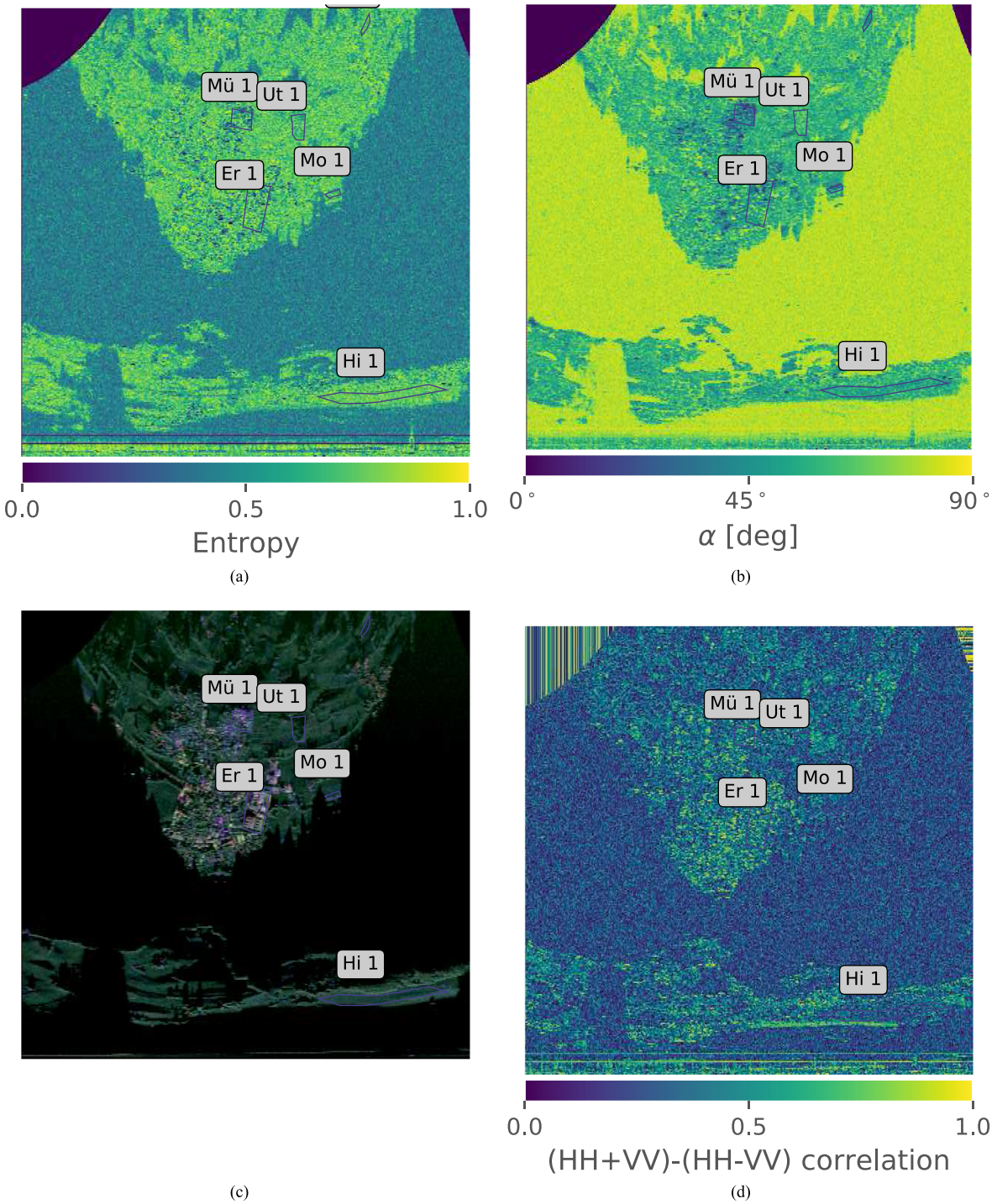

Fig. 10. (a) Cloude–Pottier entropy H, (b) mean α, (c) Pauli RGB composite, and (d) magnitude of $\gamma_{(HH-VV)-(HH+VV)}$ for the Chutzen dataset. The parameters were estimated with a 20×2 boxcar filter. (a) Cloude-Pottier entropy H. (b) Cloude-Pottier mean α angle. (c) Pauli RGB. Red: $|HH - VV|$. Green: $1/\sqrt{2}\,|HV + VH|$. Blue: $|HH + VV|$. (d) Magnitude of $\gamma_{(HH-VV)-(HH+VV)}$.

2) "Bi 2" is located on a steep mountain face. In the aerial photograph, the rock appears snow free. This is confirmed by webcam photos, showing no appearance of snow during the time-span analyzed. The bare rock surface explains the temporal and spatial stability of the polarimetric parameters. In this case, the dominant scattering mechanism is presumably medium entropy surface scattering. Given the high crosspolar power and the entropy, the surface is rougher than "Bi 1," explaining the lower $\gamma_{(HH-VV)-(HH+VV)}$ [11].

An alternative explanation for the observed entropy and α is presence of many even-bounce scattering processes in

the resolution cell, such as from single boulders smaller than the pixel's size. This corresponds to the typical mechanism behind *Zone 4: Medium Entropy Multiple Scattering* in the Cloude–Pottier classification. This hypothesis is supported by the observation of a stronger HH component compared to the VV power, as expected for even-bounce scattering.

The observed diurnal variations of backscatter power might be caused by changes in moisture content, driven by variations of solar irradiation [46], [48], [90], [91].

3) "Bi 3" is classified as glacier in the land cover map. The aerial photograph shows several crevasses and glacier ice covered in glacial till. Because of the cover and the short wavelength, appreciable penetration in the ice volume is unlikely. At *Ku*-band, a penetration depth in the order of meters is observed with very dry snow and ice [92], [93]. Considering this, the same interpretation as for "Bi 1" should apply to this case.

   The diurnal variations in backscatter power are probably related to changes in the ice surface water content, which in turn are correlated with solar radiation.

4) "Bi 4" is located on a small hanging glacier on the flanks of Weisshorn.

   Considering that the snow surface appears smooth in the aerial photograph and given the high altitude of this ROI, scattering contribution from the ice volume is more likely than in the lower ROIs as the ice is more likely to be frozen. Evidence in favor of volume scattering is the high crosspolarized backscatter and lower copolar magnitude and its broader distribution. The lower value of $\gamma_{(HH-VV)-(HH+VV)}$ compared to the other "Bi" ROIs supports this explanation: a random volume is rotationally invariant [94] and, therefore, shows lower polarimetric coherence.

5) "Lä 1" is assigned the land cover classification "Granular Soil"; this is confirmed by the aerial photographs, which show that the entire ROI only consists glacial till.

   As no vegetation is present, the two most likely mechanisms generating high entropy is multiple scattering from a dense packing of boulders [9] or surface scattering from a very rough surface. The low value of $\gamma_{(HH-VV)-(HH+VV)}$ is typical of azimuthally symmetric scattering, as expected from a random medium. The higher level of HH backscatter compared to VV would suggest the dominance of even-bounce scattering; the difference in backscatter coefficients explaining the lower copolar coherence.

   Diurnal variations in backscatter are again observed; supposedly correlated to changes in soil moisture [50], [52] driven by solar radiation.

6) "Lä 2" is classified as "Closed Forest". The a aerial photographs show a sparse forest growing on scree.

   In this case, given the surface cover, the classification in *Zone 4: Medium Entropy Multiple Scattering* seems the most reasonable. Vegetation scattering, either from the canopy volume or dihedral interactions under the canopy followed from propagation in the vegetation volume, contribute significantly to the scattering in this ROI.

   Evidence for the dominance of even bounce scattering is given by the HH component being larger than VV and by the copolar phase difference being lower with a smaller coherence magnitude. This interpretation is supported by the very low value of $\gamma_{(HH-VV)-(HH+VV)}$ that is typical of an azimuthally symmetric medium such as a vegetation volume. The low copolar coherence and its broad distribution are also suggesting high scattering randomness.

   Daily variations of backscatter are observed, which could be related to changes in vegetation water content [45], [95]–[97].

7) "Mi 1" consists entirely of short grass. The observed values of H and α would suggest a classification between *Zone 5: Medium Entropy Vegetation Scattering* and *Zone 4: Medium Entropy Multiple Scattering*; the most likely mechanism being scattering from a distribution of anisotropic scatterers with a dominant orientation. This is reasonable considering the low level of $\gamma_{(HH-VV)-(HH+VV)}$ suggesting an azimuthally symmetric distributed medium with a certain degree of randomness.

   The higher level of VV compared to HH and the low copolar phase difference point to predominantly vertically oriented structures, such as blades of grass. The considerable amount of HV backscatter suggest secondary scattering mechanisms; either rough soil or randomness in the vegetation orientation distribution, which could explain the low $\gamma_{(HH-VV)-(HH+VV)}$and copolar coherence.

   Regular diurnal variations in the total backscatter power are observed again; the most likely driver for these changes being soil moisture and vegetation water content.

In the plot of Fig. 4(b), the entropy is never below 0.5 in average all for any of the ROIs. This observation also applies to the scene as a whole: the areas of lower entropy being mostly located in proximity of the glacier and on individual pixels where a very strong scatterer is found. Similarly, the glacier is the area displaying the lowest α angle, suggesting the dominance of surface scattering, which appears blue in the Pauli RGB composite. At the same locations, $\gamma_{(HH-VV)-(HH+VV)}$ attains its highest value, which indicates a smoother surface; these observations would suggest a dominance of lower entropy surface scattering, presumably because the glacier's surface is wet during summer.

Crosspolar backscatter dominates in most of the scene, seeing as predominance of green in the Pauli RGB composite. One exception is the region at the left of "Bi 3," where a set of pixels with low entropy are seen, presumably dihedral scattering from highly reflective objects, seen as bright red pixel in the Pauli composite. Comparison with aerial photographs show the presence of avalanche protection structures.

2) Chutzen: Similarly as observed for the "Bisgletscher" dataset, a high entropy is seen for distributed targets, as displayed in Fig. 10(a). There are, however, individual pixels that display an entropy closer to zero. They correspond to bright scatterers

like single buildings, as can be seen in the Pauli RGB composite of Fig. 10(c).

Other than these exceptions, most of the scene would be again classified in the *Medium Entropy Scattering* region according to scheme proposed by Cloude and Pottier. Unlike the Bisgletscher dataset, more variability in α is observed in Fig. 10(b).

In an attempt to understand the possible physical mechanisms at the root of the observed parameters, the analysis made for the Bisgletscher observations is repeated in the following.

1) The land cover classification for "Er 1" is "Consolidated Surfaces." The very wide distribution of the Cloude–Pottier parameters, of the backscatter and $\gamma_{(HH-VV)-(HH+VV)}$ do not permit to assign a single scattering mechanism to the pixels in this ROI. This appears reasonable considering the variety of building types and orientations observed in the aerial photo Fig. 3(b).
   The low entropy pixels observed inside the ROI in Fig. 10(a) presumably correspond to scattering from buildings, which are seen as the bright points in the RGB composite [see Fig. 10(c)]. These are either direct scattering from edges or triple scattering in corners—seen as the points of low α—or odd-bounce scattering between the ground and the buildings—seen as the points where α is close to 90°.
2) "Go 1" consists of a single field and is classified as "Grass and Herb Vegetation." The Cloude–Pottier histogram is concentrated at the edge of *Zone 4: Medium Entropy Multiple Scattering*.
   This classification is compatible with the observed distribution of backscatter: in the Cloude–Pottier classification vegetation is assumed to scatter as a cloud of anisotropic, randomly oriented dipoles. The higher VV contribution and the high copolar coherence magnitude suggest a dominance of vertical structures such as stalks and blades of grass, the significant HV contribution and the high entropy are generated by a broad distribution of dipole orientation angles around the predominantly vertical orientation or by the presence of secondary scattering mechanisms, for example the combination of predominantly vertical stalks under a random canopy [98].
   $\gamma_{(HH-VV)-(HH+VV)}$ is consistent with the hypothesis of vegetation scattering since lower values are indicative of azimuthal symmetry [44].
   Another explanation for the higher VV backscatter is the effect of Bragg scattering from tilling rows the fields, which were visible to the radar after the covering vegetation was harvested [99]. The concentration of copolar phase difference close to zero, and the low $\gamma_{(HH-VV)-(HH+VV)}$ support this interpretation. Under this hypothesism the large HV contribution and the entropy are due to secondary scattering from short vegetation or to random distribution of orientations [11].
3) "Hi 1" is classified as "Grass and Herb Vegetation." The median values of H and α correspond to *Zone 4: Medium Entropy Multiple Scattering*. The crosspolar power is significantly stronger than the copolar. Compared to "Go 1," the lack of a preferential orientation in the vegetation may cause the smaller difference between HH and VV and the larger crosspolar power. The low value of $\gamma_{(HH-VV)-(HH+VV)}$ is typical of natural surfaces.
   As discussed for "Go 1" medium entropy surface scattering from a rough soil could cause the higher entropy and the wider distribution of copolar phase differences.
4) "Mo 1" is classified as "Grass and Herb Vegetation." The values of H and α correspond to *Zone 6: Medium Entropy Surface Scattering* in the Cloude–Pottier plane. In this case, the median copolar backscatter is higher than the crosspolar and α is lower; this suggests surface scattering from a smooth surface. The low $\gamma_{(HH-VV)-(HH+VV)}$ and the high copolar coherence magnitude and narrow, zero-mean copolar phase difference distribution are consistent with this explanation.
   Given the date of acquisition, this appears plausible since summer crops would have been harvested, leaving bare soil exposed.
5) "Mü 1" is located on a residential area. The distribution of α and H is very wide and does not allow the assignment of a single scattering mechanism to this ROI.
   Likewise, the ROI contains a mixture of many scattering types, from low entropy scattering by buildings to vegetation scatter from trees and gardens. An interesting observation is a peak in the HV power approximately 5 dB lower than the copolar peak: perhaps the weaker secondary scattering from vegetated surfaces, whose radar cross section is considerably smaller than the highly reflective buildings.
6) "Ut 1" covers a forest. The Cloude–Pottier parameters indicate a classification in *Zone 4: Medium Entropy Multiple Scattering*. However, double bounces followed by propagation in the vegetation volume seems rather unlikely considering the very shallow incidence angle, where penetration into the forest appears difficult, and the very similar HH and VV powers.
   Most of the scattering is from the vegetation canopy, which appears either as a very rough surface or as a random volume, depending on the penetration depth. $\gamma_{(HH-VV)-(HH+VV)}$ is observed to be low, suggesting an azimuthally symmetrical volume.
   The low copolar coherence magnitude is typical of random volumes, as is the wide distribution of copolar phase differences [100].

In the case of the Chutzen dataset, the entropy appears to be slightly lower than observed for the Bisgletscher data. This may be due to the small slant range distance of the scene, leading to a reduced noise level. The corrected antenna pattern mispointing also contributes to this by increasing the SNR by 1.8 dB.

Some points with very low entropy can be seen in near range and at the middle of the scene: they correspond to individual houses or to the trihedral corner reflectors. These are visible in the α map as well, as it is very close to zero for odd-bounce scattering. In the case of built-up areas, the main interaction can be expected to be either direct scattering from the edges of

buildings or double-bounce scattering between the walls and the ground.

The high entropy and α observed in the rest of the scene suggest that the main dominant scattering mechanism corresponds to *Zone 4: Medium Entropy Multiple Scattering*. This is compatible with the observed $\gamma_{(HH-VV)-(HH+VV)}$, which is low except at low-entropy pixels. Since the land cover class of most of the scene is either pasture, farmland or forest, it is reasonable to expect medium entropy surface scattering to be the most dominant contribution: these surfaces are presumably azimuthally symmetrical, as it can be expected for most natural surfaces.

B. Other Causes of Entropy Increase

Other than depolarizing scattering as described above, the presence of measurement noise, the process of multilooking and the imaging resolution can cause increased value of entropy even in the absence of depolarizing scattering.

The effect of measurement noise on the observed entropy was assessed by estimating the noise equivalent radar cross section (NESZ) from 50 acquisitions in the Bisgletscher dataset, using the pixels located in areas of radar shadow. The result of this analysis show that the crosspolar channels—HV and VH—have an NESZ 10 dB larger than the copolar channels.

It appears that for measurements made with KAPRI, noise does not significantly increase entropy. This can be seen in the entropy maps and Pauli RGB composites. In areas affected by radar shadow, for example immediately on top of the "Bi 1" ROI, the entropy is lower, closer to 0.6. This is due to the noise imbalance between the copolar and the crosspolar channels.

A simulation, was performed by generating 1000 realizations of multivariate colored Gaussian noise with the HV power 10 dB stronger than both VV and HH and adding the noise to a zero-entropy scattering vector. From this vector, $\mathbf{T}$ was estimated by averaging over the realizations of the noise. The result of this simulation was an entropy of 0.6; very close to the entropy estimated in areas affected radar shadows.

A comparison of entropy estimate for the Bisgletscher dataset is displayed in Fig. 7. In Fig. 7(a), H_{boxcar} is shown, Fig. 7(b) displays the temporal estimate H_{temporal}, and Fig. 7(c) displays H_{IDAN} for the same dataset. The same comparison is not possible for the Chutzen dataset because no time series is available.

The entropy obtained with the IDAN filter, H_{IDAN} is lower than the entropy estimated with the boxcar average H_{boxcar}. However, both methods show the same contrast between different areas and land cover types. On the contrary, H_{IDAN} appears grainier and spatially less smooth. The difference between the glacier and the surrounding rocks seems to be lower in H_{IDAN} than in H_{boxcar}, where near "Bi 3" the difference is visible and reflected by the change between green and blue in the Pauli RGB composite. The lower entropy contrast of the IDAN filter may be due to the filter's implementations, as only backscatter power and not the polarimetric information is used to test the similarity of pixels that are deemed to belong to the same region for averaging. Thus, in some cases the IDAN filter might not be able to reduce spatial mixing; for example at the edges where two different scattering types with similar total backscatter power meet.

The temporal entropy H_{temporal} is much lower than both H_{boxcar} and H_{IDAN}, in correspondence with the glacier. The glacier's outline can be seen as it contrasts with the surrounding rocks left of the "Bi 3" ROI.

However, this observation is not sufficient to prove that spatial mixing is the only factor causing of high entropy. The glacier's high flow velocity—up to $2\mathrm{m}/\mathrm{day}$—and weather-driven changes in the ice surface are likely to cause changes in the scattering response, thereby increasing H_{temporal}.

The entropy of rocky areas next to the "Lä" ROIs may be underestimated by H_{temporal}. The dominance of HV backscatter is connected to depolarizing scattering; it is unlikely that natural scatterers on such a large scale have the same orientation and act as crosspolarizers [72] that can produce significant HV backscatter.

Thus, if the presence of depolarizing scattering is assumed, the temporal stability of the scattering response for individual pixels is the cause of the discrepancy between H_{temporal} and the spatial entropy estimates H_{boxcar}.

As an example, if the X-Bragg scattering model [11] is used to explain the scattering for a certain pixel and if its surface properties and roughness do not change over time—as it likely the case for rough, dry soil over the course of a few hours—then the observed scattering matrix will remain the same up to a noise contribution and temporal estimation of the entropy will give low values, effectively hiding the depolarization.

Ergodicity does not apply in this case. Averaging the coherency matrix for a single pixel over time is not equivalent to the average of coherency matrices of individual facets over the distribution of orientation angles.

The same arguments apply to volume scattering. If dielectric properties, shape, and orientation of particles in a random volume do not change in time, the entropy estimated with temporal averaging will be very low even though the scattering process is depolarizing in a strict sense, that is when the entropy is estimated over the distribution of the particles [44]. Unfortunately, this cannot be observed. For vegetated areas as "Mi 1", the effect of wind and changes in vegetation water content are so large to modify the scattering properties of vegetation, causing a high H_{temporal}.

This analysis suggests that, depending on the type of target and the acquisition repeat time and geometry, neither temporal nor spatial averages are completely adequate to estimate entropy.

Since H_{temporal} is very sensitive to changes in the scattering properties, its adequacy to characterize depolarizing scattering processes is doubtful when the average is performed using images far apart in time: the samples over which the average is made do not strictly represent the same objects anymore if the surface undergoes large changes, which is very plausible for the glacier's surface or vegetated areas.

Similarly, the spatial estimators suffer from spatial mixing and resolution loss, which can be especially problematic at the low resolution of TRIs, since a large enough number of samples needs to be averaged for a robust estimate.

V. Conclusion

This article presents an analysis of *Ku*-band polarimetric data from two test sites, acquired with the KAPRI polarimetric terrestrial radar. The first dataset is a time series of the Bisgletscher, an Alpine glacier in the Swiss Alps, acquired in the summer of 2015. The other dataset was acquired in September 2016 in an agricultural area near Münsingen, Canton of Bern, Switzerland.

The most relevant observation made for both datasets is a high Cloude–Pottier entropy parameter H; higher than 0.5 for natural targets and only observed to be close to 0 for highly reflective scatterers such as buildings or trihedral corner reflectors.

The high entropy is accompanied by an α angle above 50° and a high fraction of crosspolarized backscatter. These values hint at the dominance of depolarizing scattering mechanisms. This interpretation is realistic in the light of the dominance of natural surfaces in both scenes. In alternative to this explanation, effects other than depolarizing scattering can bias the observed entropy [64], [72].

1) Thermal noise in the radar electronics: This is less likely because of the imbalance in polarimetric noise.
2) The spatial average used to estimate the coherency matrix may bias the entropy if the scene is very heterogeneous and spatially adjacent pixels do not represent realizations of the same extended target [64].
   This has been tested by comparing different averaging methods (temporal average, boxcar, and IDAN filter), which gave similar results excepts in areas affected by fast changes. Thus, again mixing is not likely to cause the high entropy.
3) Another source of increased entropy is the relationship of the resolution cell size to the wavelength, having a ratio of 1000 in this case. Thus, several scatterers are present in a resolution cell, increasing the entropy. This calls for detailed investigation by imaging the same distributed target at different wavelengths with similar resolutions.
4) Finally, the effect of incidence angle should also be considered. It is known that for steeper incidence angles the scattering tends to be less diffuse, and thus, a lower level of depolarization,and hence, a lower entropy should be observed [101], [102]. In TRI, usually very shallow incidence angles are employed, which could contribute to the increase of the observed entropy.

References

[1] R. F. Hanssen, *Radar Interferometry* (ser. Remote Sensing and Digital Image Processing), vol. 2. Netherlands: Springer, 2001. [Online]. Available: http://www.iub.edu/~act/files/publications/2004/04-12_LUCCPathways_Impacts.pdfhttp://link.springer.com/10.1007/0-306-47633-9http://www.nature.com/doifinder/10.1038/scientificamerican0297-46

[2] D. Massonnet and K. L. Feigl, "Radar interferometry and its application to changes in the earth's surface," *Rev. Geophys.*, vol. 36, pp. 441–500, Nov. 1998.

[3] R. Horn, A. Nottensteiner, A. Reigber, J. Fischer, and R. Scheiber, "F-SAR—DLR's new multifrequency polarimetric airborne SAR," in *Proc. IEEE Int. Geosci. Remote Sens. Symp.*, 2009, vol. 2, pp. II–902.

[4] S. Angelliaume, P. Dubois-Fernandez, P. Dreuillet, H. Oriot, and C. Coulombeix, "SETHI, the ONERA airborne SAR sensor, and his low frequency capability," in *Proc. IEEE Int. Geosci. Remote Sens. Symp.*, 2009, vol. 4, pp. IV–177.

[5] J. van Zyl, R. Carande, Y. Lou, T. Miller, and K. Wheeler, "The NASA/JPL three-frequency polarimetric AIRSAR system," *Proc. IEEE Int. Geosci. Remote Sens. Symp.*, Houston, TX, USA, 1992, pp. 649–651.

[6] P. Rosen *et al.*, "UAVSAR: New NASA airborne SAR system for research," *IEEE Aerosp. Electron. Syst. Mag.*, vol. 22, no. 11, pp. 21–28, Nov. 2007.

[7] A. Rosenqvist, M. Shimada, and M. Watanabe, "ALOS PALSAR: Technical outline and mission concepts," in *Proc. Int. Symp. Retrieval Bio-Geophys. Parameters SAR Data Land Appl.*, 2004, vol. 1, pp. 1–7.

[8] L. C. Morena, K. V. James, and J. Beck, "An introduction to the RADARSAT-2 mission," *Can. J. Remote Sens.*, vol. 30, pp. 221–234, 2004.

[9] S. Cloude and E. Pottier, "An entropy based classification scheme for land applications of polarimetric SAR," *IEEE Trans. Geosci. Remote Sens.*, vol. 35, no. 1, pp. 68–78, Jan. 1997.

[10] J.-S. Lee, M. Grunes, T. Ainsworth, L.-J. Du, D. Schuler, and S. Cloude, "Unsupervised classification using polarimetric decomposition and the complex Wishart classifier," *IEEE Trans. Geosci. Remote Sens.*, vol. 37, no. 5, pp. 2249–2258, Sep. 1999.

[11] I. Hajnsek, E. Pottier, and S. Cloude, "Inversion of surface parameters from polarimetric SAR," *IEEE Trans. Geosci. Remote Sens.*, vol. 41, no. 4, pp. 727–744, Apr. 2003.

[12] F. T. Ulaby, D. Held, M. C. Donson, K. C. McDonald, and T. B. A. Senior, "Relating polarization phase difference of SAR signals to scene properties," *IEEE Trans. Geosci. Remote Sens.*, vol. GE-25, no. 1, pp. 83–92, Jan. 1987. [Online]. Available: http://ieeexplore.ieee.org/lpdocs/epic03/wrapper.htm?arnumber=4072602

[13] S. Leinss, G. Parrella, and I. Hajnsek, "Snow height determination by polarimetric phase differences in *X*-band SAR data," *IEEE J. Sel. Topics Appl. Earth Observ. Remote Sens.*, vol. 7, pp. 3794–3810, Sep. 2014. [Online]. Available: http://ieeexplore.ieee.org/lpdocs/epic03/wrapper.htm?arnumber=6841006

[14] K. Papathanassiou and S. Cloude, "Single-baseline polarimetric SAR interferometry," *IEEE Trans. Geosci. Remote Sens.*, vol. 39, no. 11, pp. 2352–2363, 2001. [Online]. Available: http://ieeexplore.ieee.org/lpdocs/epic03/wrapper.htm?arnumber=964971

[15] S. Cloude, J. Fortuny, J. Lopez-Sanchez, and A. Sieber, "Wide-band polarimetric radar inversion studies for vegetation layers," *IEEE Trans. Geosci. Remote Sens.*, vol. 37, no. 5, pp. 2430–2441, Sep. 1999.

[16] G. Parrella, I. Hajnsek, and K. P. Papathanassiou, "Polarimetric decomposition of *L*-band PolSAR backscattering over the Austfonna ice cap," *IEEE Trans. Geosci. Remote Sens.*, vol. 54, no. 3, pp. 1267–1281, Mar. 2016.

[17] I. Hajnsek, "Inversion of surface parameters using polarimetric SAR," Ph.D. dissertation, Friedrich-Schiller-Universität Jena, Jena, Germany, Apr. 2001. [Online]. Available: https://www.db-thueringen.de/servlets/MCRFileNodeServlet/dbt_derivate_0 0001090/diss_hajnsek.pdf

[18] S. Brown and J. Bennett, "High-resolution microwave polarimetric imaging of small trees," *IEEE Trans. Geosci. Remote Sens.*, vol. 37, no. 1, pp. 48–53, Jan. 1999.

[19] K. Morrison, J. Bennett, and S. Solberg, "Ground-based *C*-band tomographic profiling of a conifer forest stand," *Int. J. Remote Sens.*, vol. 34, pp. 7838–7853, Sep. 2013.

[20] R. Caduff and T. Strozzi, "Terrestrial radar interferometry monitoring during a landslide emergency 2016, Ghirone, Switzerland," in *Advancing Culture of Living With Landslides*. Berlin, Germany: Springer, 2017, pp. 301–309. [Online]. Available: https://doi.org/10.1007/978-3-319-53487-9_34

[21] O. Monserrat, M. Crosetto, and G. Luzi, "A review of ground-based SAR interferometry for deformation measurement," *ISPRS J. Photogrammetry Remote Sens.*, vol. 93, pp. 40–48, Jul. 2014.

[22] G. Luzi *et al.*, "Ground-based radar interferometry for landslides monitoring: Atmospheric and instrumental decorrelation sources on experimental data," *IEEE Trans. Geosci. Remote Sens.*, vol. 42, no. 11, pp. 2454–2466, Nov. 2004.

[23] S. Rödelsperger, G. Läufer, C. Gerstenecker, and M. Becker, "Monitoring of displacements with ground-based microwave interferometry: IBIS-S and IBIS-L," *J. Appl. Geodesy*, vol. 4, pp. 41–54, Jan. 2010.

[24] J. Butt, A. Wieser, and S. Conzett, "Intrinsic random functions for mitigation of atmospheric effects in terrestrial radar interferometry," *J. Appl. Geodesy*, vol. 11, pp. 89–98, Jan. 2017.

[25] L. Pipia, X. Fabregas, A. Aguasca, and C. Lopez-Martinez, "Polarimetric temporal analysis of urban environments with a ground-based SAR," *IEEE Trans. Geosci. Remote Sens.*, vol. 51, no. 4, pp. 2343–2360, Apr. 2013.

[26] L. Noferini, D. Mecatti, G. Macaluso, M. Pieraccini, and C. Atzeni, "Monitoring of Belvedere Glacier using a wide angle GB-SAR interferometer," *J. Appl. Geophys.*, vol. 68, pp. 289–293, Jun. 2009.

[27] R. Caduff, F. Schlunegger, A. Kos, and A. Wiesmann, "A review of terrestrial radar interferometry for measuring surface change in the geosciences," *Earth Surf. Processes Landforms*, vol. 40, pp. 208–228, Oct. 2014.

[28] R. Iglesias *et al.*, "Ground-based polarimetric SAR interferometry for the monitoring of terrain displacement phenomena–part I: Theoretical description," *IEEE J. Sel. Topics Appl. Earth Observ. Remote Sens.*, vol. 8, pp. 1–1, 2014. [Online]. Available: http://ieeexplore.ieee.org/lpdocs/epic03/wrapper.htm?arnumber=6981929http://ieeexplore.ieee.org/lpdocs/epic03/wrapper.htm?arnumber=6982213

[29] L. Pipia, X. Fabregas, A. Aguasca, C. Lopez-Martinez, J. J. Mallorqui, and O. Moraline, "Polarimetric temporal information for urban deformation map retrieval," in *Proc. IEEE Int. Geosci. Remote Sens. Symp.*, 2007, pp. 192–195.

[30] A. Aguasca, A. Broquetas, J. Mallorque, and X. Fabregas, "A solid state *L* to *X*-band flexible ground-based SAR system for continuous monitoring applications," in *Proc. IEEE Int. Geosci. Remote Sens. Symp.*, 2004, vol. 2, pp. 757–760. [Online]. Available: http://ieeexplore.ieee.org/xpls/abs_all.jsp?arnumber=1368512%5Cnh% ttp://ieeexplore.ieee.org/lpdocs/epic03/wrapper.htm?arnumber=1368512

[31] L. Pipia, X. Fabregas, A. Aguasca, C. Lopez-Martinez, J. J. Mallorqui, and O. Mora, "A subsidence monitoring project using a polarimetric GB-SAR sensor," in *Proc. PolInSAR*, 2009, pp. 22–26.

[32] R. Iglesias *et al.*, "Ground-based polarimetric SAR interferometry for the monitoring of terrain displacement phenomena–Part II: Applications," *IEEE J. Sel. Topics Appl. Earth Observ. Remote Sens.*, vol. 8, no. 3, pp. 994–1007, Jul. 2013.

[33] R. Iglesias, D. Monells, X. Fabregas, J. J. Mallorqui, A. Aguasca, and C. Lopez-Martinez, "Phase quality optimization in polarimetric differential SAR interferometry," *IEEE Trans. Geosci. Remote Sens.*, vol. 52, no. 5, pp. 2875–2888, May 2014.

[34] H. Lee, S.-J. Cho, N.-H. Sung, and J.-H. Kim, "Development of a ground-based synthetic aperture radar system for highly repeatable measurements," in *Proc. 9th Workshop Subsurface Electromagn. Meas.*, 2007, pp. 2–6. [Online]. Available: http://sar.kangwon.ac.kr/paper/sem_gbsar.pdf

[35] M.-K. Kang, K.-E. Kim, H. Lee, S.-J. Cho, and J.-H. Lee, "Preliminary result of polarization property analysis using fully polarimetric GB-SAR images," in *Proc. IEEE Int. Geosci. Remote Sens. Symp.*, Jul. 2010, pp. 4019–4022. [Online]. Available: http://ieeexplore.ieee.org/xpls/abs_all.jsp?arnumber=5650762http://ieeexplore.ieee.org/lpdocs/epic03/wrapper.htm?arnumber=5650762

[36] M.-K. Kang, K.-E. Kim, H. Lee, S.-J. Cho, and J.-H. Lee, "Preliminary results of polarimetric characteristics for *C*-band quad-polarization GB-SAR images using H / A / α polarimetric decomposition theorem," vol. 25, pp. 531–546, 2009.

[37] J. Bennett, K. Morrison, A. Race, G. Cookmartin, and S. Quegan, "The UK NERC fully portable polarimetric ground-based synthetic aperture radar (GB-SAR)," in *Proc. IEEE Eur. Conf. Synthetic Aperture Radar*, 2000, pp. 2313–2315.

[38] J. Bennett and K. Morrison, "Development of a ground-based, polarimetric synthetic aperture radar," in *Proc. IEEE Aerosp. Appl. Conf.*, 1996, vol. 4, pp. 139–146.

[39] S. Brown, S. Quegan, K. Morrison, J. Bennett, and G. Cookmartin, "High-resolution measurements of scattering in wheat canopies-implications for crop parameter retrieval," *IEEE Trans. Geosci. Remote Sens.*, vol. 41, no. 7, pp. 1602–1610, Jul. 2003.

[40] S. Zwieback, S. Hensley, and I. Hajnsek, "A polarimetric first-order model of soil moisture effects on the DInSAR coherence," *Remote Sens.*, vol. 7, pp. 7571–7596, Jun. 2015. [Online]. Available: http://www.mdpi.com/2072-4292/7/6/7571/

[41] S. Baffelli, O. Frey, C. Werner, and I. Hajnsek, "Polarimetric calibration of the *Ku*-band advanced polarimetric radar interferometer," *IEEE Trans. Geosci. Remote Sens.*, vol. 56, no. 4, pp. 2295–2311, Apr. 2018. [Online]. Available: http://ieeexplore.ieee.org/document/8226855/

[42] S. Cloude and E. Pottier, "A review of target decomposition theorems in radar polarimetry," *IEEE Trans. Geosci. Remote Sens.*, vol. 34, no. 2, pp. 498–518, Mar. 1996. [Online]. Available: http://ieeexplore.ieee.org/xpls/abs_all.jsp?arnumber=485127

[43] S. Cloude, "A new method for characterizing depolarization effects in radar and optical remote sensing," in *Proc. IEEE Int. Geosci. Remote Sens. Symp.*, 2001, pp. 910–912

[44] S. Cloude, *Polarisation: Applications in Remote Sensing*. London, U.K.: Oxford Univ. Press, Oct. 2009.

[45] T. van Emmerik, S. C. Steele-Dunne, J. Judge, and N. van de Giesen, "Impact of diurnal variation in vegetation water content on radar backscatter from maize during water stress," *IEEE Trans. Geosci. Remote Sens.*, vol. 53, no. 7, pp. 3855–3869, Jul. 2015.

[46] J. Shi, C. Xiong, and L. Jiang, "Review of snow water equivalent microwave remote sensing," *Sci. China Earth Sci.*, vol. 59, pp. 731–745, Jan. 2016.

[47] J. Shi, "Snow water equivalence retrieval using *X* and *Ku* band dual-polarization radar," in *Proc. IEEE Int. Geosci. Remote Sens. Symp.*, Jul. 2006, pp. 2183–2185.

[48] F. T. Ulaby and W. H. Stiles, "The active and passive microwave response to snow parameters: 2. water equivalent of dry snow," *J. Geophys. Res.*, vol. 85, pp. 1045–1049, 1980.

[49] T. Strozzi and C. Mätzler, "Backscattering measurements of Alpine snowcovers at 5.3 and 35 GHz," *IEEE Trans. Geosci. Remote Sens.*, vol. 36, no. 3, pp. 838–848, May 1998.

[50] F. Ulaby, P. Batlivala, and M. Dobson, "Microwave backscatter dependence on surface roughness, soil moisture, and soil texture: Part I-bare soil," *IEEE Trans. Geosci. Electron.*, vol. GE-16, no. 4, pp. 286–295, Oct. 1978.

[51] K. Sarabandi, Y. Oh, and F. Ulaby, "Polarimetric radar measurements of bare soil surfaces at microwave frequencies," in *Proc. IEEE Int. Geosci. Remote Sens. Symp.*, 1991, vol. 2, pp. 387–390.

[52] W. Wagner *et al.*, "Temporal stability of soil moisture and radar backscatter observed by the advanced synthetic aperture radar (ASAR)," *Sensors*, vol. 8, pp. 1174–1197, Feb. 2008.

[53] T. A. Seliga and V. N. Bringi, "Differential reflectivity and differential phase shift: Applications in radar meteorology," *Radio Sci.*, vol. 13, no. 2, pp. 271–275, Mar./Apr. 1978.

[54] G. Parrella, I. Hajnsek, and K. P. Papathanassiou, "On the interpretation of polarimetric phase differences in SAR data over land ice," *IEEE Geosci. Remote Sens. Lett.*, vol. 13, no. 2, pp. 192–196, Feb. 2016. [Online]. Available: http://ieeexplore.ieee.org/lpdocs/epic03/wrapper.htm?arnumber=7362141

[55] E. Pottier and S. R. Cloude, "Unsupervised classification of full polarimetric SAR data and feature vectors identification using radar target decomposition theorems and entropy analysis," in *Proc. IEEE Int. Geosci. Remote Sens. Symp.*, 1995, vol. 3, pp. 2247–2249.

[56] A. Freeman and S. Durden, "A three-component scattering model for polarimetric SAR data," *IEEE Trans. Geosci. Remote Sens.*, vol. 36, no. 3, pp. 963–973, May 1998.

[57] S. Ito, T. Oguchi, T. Iguchi, H. Kumagai, and R. Meneghini, "Depolarization of radar signals due to multiple scattering in rain," *IEEE Trans. Geosci. Remote Sens.* vol. 33, no. 4, pp. 1057–1062, Jul. 1995.

[58] R. T. Shin and J. A. Kong, "Radiative transfer theory for active remote sensing of a homogenous layer containing spherical scatterers," *J. Appl. Phys.*, vol. 52, no. 6, pp. 4221–4230, Jun. 1981.

[59] D. Bicout and C. Brosseau, "Multiply scattered waves through a spatially random medium: Entropy production and depolarization," *J. de Physique I*, vol. 2, no. 11, pp. 2047–2063, Nov. 1992.

[60] M. Boregaud and J. Noll, "Analysis of theoretical surface scattering models for polarimetric microwave remote sensing of bare soils," *Int. J. Remote Sens.*, vol. 15, pp. 2931–2942, Sep. 1994.

[61] M. F. Chen and A. K. Fung, "A numerical study of the regions of validity of the Kirchhoff and small-perturbation rough surface scattering models," *Radio Sci.*, vol. 23, pp. 163–170, Mar. 1988.

[62] S.-B. Kim, H. Huang, T.-H. Liao, and A. Colliander, "Estimating vegetation water content and soil surface roughness using physical models of *L*-band radar scattering for soil moisture retrieval," *Remote Sens.*, vol. 10, no. 4, Apr. 2018, Art. no. 556.

[63] S.-E. Park, W. M. Moon, and D. Jin Kim, "Estimation of surface roughness parameter in intertidal mudflat using airborne polarimetric SAR data," *IEEE Trans. Geosci. Remote Sens.*, vol. 47, no. 4, pp. 1022–1031, Apr. 2009.

[64] F. Weissgerber, E. Colin-Koeniguer, N. Trouve, and J.-M. Nicolas, "A temporal estimation of entropy and its comparison with spatial estimations on PolSAR images," *IEEE J. Sel. Topics Appl. Earth Observ. Remote Sens.*, vol. 9, no. 8, pp. 3809–3820, Aug. 2016.

[65] J.-S. Lee, T. L. Ainsworth, J. Kelly, and C. Lopez-Martinez, "Evaluation and bias removal of multi-look effect on entropy/alpha/anisotropy," in *Proc. IEEE Int. Geosci. Remote Sens. Symp.*, 2007, pp. 172–175.

[66] J.-S. Lee, M. Grunes, and G. de Grandi, "Polarimetric SAR speckle filtering and its implication for classification," *IEEE Trans. Geosci. Remote Sens.*, vol. 37, no. 5, pp. 2363–2373, Sep. 1999.

[67] J. Chen, Y. Chen, W. An, Y. Cui, and J. Yang, "Nonlocal filtering for polarimetric SAR data: A pretest approach," *IEEE Trans. Geosci. Remote Sens.*, vol. 49, no. 5, pp. 1744–1754, May 2011.
[68] C.-A. Deledalle, F. Tupin, and L. Denis, "Polarimetric SAR estimation based on non-local means," in *Proc. IEEE Int. Geosci. Remote Sens. Symp.*, Jul. 2010, pp. 2515–2518.
[69] S. Parrilli, M. Poderico, C. Angelino, G. Scarpa, and L. Verdoliva, "A nonlocal approach for SAR image denoising," in *Proc. IEEE Int. Geosci. Remote Sens. Symp.*, Jul. 2010, pp. 726–729. [Online]. Available: http://ieeexplore.ieee.org/xpls/abs_all.jsp?arnumber=5651432
[70] A. Alonso-González, C. López-Martínez, P. Salembier, and X. Deng, "Bilateral distance based filtering for polarimetric SAR data," *Remote Sens.*, vol. 5, pp. 5620–5641, Oct. 2013.
[71] G. Vasile, E. Trouve, J.-S. Lee, and V. Buzuloiu, "Intensity-driven adaptive-neighborhood technique for polarimetric and interferometric SAR parameters estimation," *IEEE Trans. Geosci. Remote Sens.*, vol. 44, no. 6, pp. 1609–1621, Jun. 2006.
[72] E. Koeniguer Colin, F. Weissgerber, N. Trouvé, and J. Nicolas, "A new light on origins of polarimetric misclassification of the SOMA district, due to the difficulty to predict entropy," in *Proc. PolInSAR*, 2015, vol. 729, pp. 1–7.
[73] C. Werner, T. Strozzi, A. Wiesmann, and U. Wegmüller, "A real-aperture radar for ground-based differential interferometry," in *Proc. IEEE Int. Geosci. Remote Sens. Symp.*, 2008, pp. 210–213.
[74] A. Meta, "Signal processing of FMCW synthetic aperture radar data," Ph.D. dissertation, Elect. Eng., Math. Comput. Sci., 2006. [Online]. Available: https://repository.tudelft.nl/islandora/object/uuid 9-87d4-4d9d8968ed81
[75] A. Stove, "Linear FMCW radar techniques," *IEE Proc. F Radar Signal Process.*, vol. 139, pp. 343–350, 1992.
[76] B. Sarkar, R. Roy, and C. Reddy, "Deterioration in resolution of a radar using long slotted waveguide antenna," in *Proc. Dig. Antennas Propag. Soc. Int. Symp.*, 1989, pp. 1740–1742. [Online]. Available: http://ieeexplore.ieee.org/lpdocs/epic03/wrapper.htm?arnumber=135070
[77] O. Frey, E. H. Meier, and D. R. Nüesch, "Processing SAR data of rugged terrain by time-domain back-projection," in *Proc. SAR Image Anal., Model., Techn. VII*, Oct. 2005, vol. 5980, pp. 598 007–598 007–9. [Online]. Available: http://proceedings.spiedigitallibrary.org/data/Conferences/SPIEP/30165/598007_1.pdfhttp://proceedings.spiedigitallibrary.org/proceeding.aspx?articleid=879695
[78] O. Frey, M. Santoro, C. L. Werner, and U. Wegmuller, "DEM-based SAR pixel-area estimation for enhanced geocoding refinement and radiometric normalization," *IEEE Geosci. Remote Sens. Lett.*, vol. 10, no. 1, pp. 48–52, Jan. 2013.
[79] M. Raymond, M. Wegmann, and M. Funk, "Inventar gefährlicher Gletscher in der Schweiz," (Mitteilungen der Versuchsanstalt für Wasserbau, Hydrologie und Glaziologie Eidgenossische Technische Hochschule) ETH Zurich, Tech. Rep. 182, 2003. [Online]. Available: http://cat.inist.fr/?aModele=afficheN&cpsidt=15381742
[80] J. Beutel, B. Buchli, F. Ferrari, M. Keller, M. Zimmerling, and L. Thiele, "X-SENSE: Sensing in extreme environments," in *Proc. Design, Automat. Test Europe*, Mar. 2011, pp. 1–6. [Online]. Available: http://ieeexplore.ieee.org/lpdocs/epic03/wrapper.htm?arnumber=5763236http://ieeexplore.ieee.org/search/srchabstract.jsp?tp=&arnumber=5763236&queryText%3D%28sensing+in+extreme+environments%29%26openedRefin ements%3D*%26matchBoolean%3Dtrue%26rowsPerPage%3D3
[81] P. Di Tommaso, M. Chatzou, E. W. Floden, P. P. Barja, E. Palumbo, and C. Notredame, "Nextflow enables reproducible computational workflows," *Nature Biotechnology*, vol. 35, pp. 316–319, Apr. 2017.
[82] Federal Office for Topography (Swisstopo). "Swissimage: The digital orthophotomosaic of Switzerland." [Online]. Available: https://www.geocat.ch/geonetwork/srv/en/catalog.search#/metadata/db5a52b4-0f5f-4998-a9a8-dd9539f93809
[83] Swiss Federal Statistical Office. "Land use statistics 2004/09 based on the land coverage nomenclature NOLC04." [Online]. Available: https://www.geocat.ch/geonetwork/srv/eng/catalog.search#/metadata/b53c03bb-a168-491f-b266-c7e9ec0af320
[84] Federal Office for Topography (Swisstopo). "Geographical names swissNAMES3D." [Online]. Available: https://www.geocat.ch/geonetwork/srv/eng/catalog.search#/metadata/ab24e5cc-7f53-451a-820a-f113fa545943
[85] Federal Office for Topography (Swisstopo). "Swissalti 3D digital elevation model." [Online]. Available: https://www.swisstopo.admin.ch/en/home/products/height/alti3d.html
[86] O. Frey, C. L. Werner, R. Caduff, and A. Wiesmann, "A time series of SAR tomographic profiles of a snowpack," in *Proc.11th Eur. Conf. Synthetic Aperture Radar*, 2016, pp. 726–730.
[87] O. Frey, C. L. Werner, R. Caduff, and A. Wiesmann, "A time series of tomographic profiles of a snow pack measured with SnowScat at *X-/Ku*-band," in *Proc. IEEE Int. Geosci. Remote Sens. Symp.*, 2016, pp. 17–20.
[88] O. Frey, C. L. Werner, and A. Wiesmann, "Tomographic profiling of the structure of a snow pack at *X-/Ku*-band using SnowScat in SAR mode," in *Proc. Eur. Radar Conf.*, Sep. 2015, vol. 1, pp. 1–4. [Online]. Available: http://ieeexplore.ieee.org/lpdocs/epic03/wrapper.htm?arnumber=7346227
[89] J. M. Lopez-Sanchez, J. D. Ballester-Berman, and S. R. Cloude, "Monitoring and retrieving rice phenology by means of satellite SAR polarimetry at *X*-band," in *Proc. IEEE Int. Geosci. Remote Sens. Symp.*, Jul. 2011, pp. 2741–2744.
[90] W. H. Stiles and F. T. Ulaby, "The active and passive microwave response to snow parameters: 1. Wetness," *J. Geophys. Res.*, vol. 85, 1980, Art. no. 1037.
[91] C. Mätzler, "Applications of the interaction of microwaves with the natural snow cover," *Remote Sens. Rev.*, vol. 2, pp. 259–387, Jan. 1987.
[92] R. Willatt, K. Giles, S. Laxon, L. Stone-Drake, and A. Worby, "Field investigations of *Ku*-band radar penetration into snow cover on antarctic sea ice," *IEEE Trans. Geosci. Remote Sens.*, vol. 48, no. 1, pp. 365–372, Jan. 2010.
[93] R. Willatt, S. Laxon, K. Giles, R. Cullen, C. Haas, and V. Helm, "*Ku*-band radar penetration into snow cover on arctic sea ice using airborne data," *Ann. Glaciology*, vol. 52, pp. 197–205, 2011.
[94] J.-S. Lee and E. Pottier, *Polarimetric Radar Imaging: From Basics To Applications*. Boca Raton, FL, USA: CRC Press.
[95] B. Brisco, R. Brown, K. J., G. Sofko, and M. Mckibben, "The diurnal pattern of microwave backscattering by wheat," *Remote Sens. Environ.*, vol. 34, pp. 37–47, Oct. 1990.
[96] M. Satake and H. Hanado, "Diurnal change of Amazon rain forest σ^0 observed by *Ku*-band spaceborne radar," *IEEE Trans. Geosci. Remote Sens.*, vol. 42, no. 6, pp. 1127–1134, Jun. 2004.
[97] E. P. W. Attema and F. T. Ulaby, "Vegetation modeled as a water cloud," *Radio Sci.*, vol. 13, pp. 357–364, Mar. 1978.
[98] M. Pichierri, I. Hajnsek, S. Zwieback, and B. Rabus, "On the potential of polarimetric SAR interferometry to characterize the biomass, moisture and structure of agricultural crops at *L*-, *C*- and *X*-bands," *Remote Sens. Environ.*, vol. 204, pp. 596–616, Jan. 2018.
[99] H. McNairn, C. Duguay, B. Brisco, and T. J. Pultz, "The effect of soil and crop residue characteristics on polarimetric radar response," *Remote Sens. Environ.*, vol. 80, pp. 308–320, May 2002.
[100] D. Evans, T. Farr, J. van Zyl, and H. Zebker, "Radar polarimetry: Analysis tools and applications," *IEEE Trans. Geosci. Remote Sens.*, vol. 26, no. 6, pp. 774–789, Nov. 1988.
[101] D. Massonnet and J.-C. Souyris, *Imaging With Synthetic Aperture Radar*. Lausanne, Switzerland: EPFL Press, 2008.
[102] J. Lopez-Sanchez, J. Fortuny-Guasch, S. Cloude, and A. Sieber, "Indoor polarimetric radar measurements on vegetation samples at *L*, *S*, *C* and *X* band," *J. Electromagn. Waves Appl.*, vol. 14, no. 2, pp. 205–231, Jan. 2000.

Simone Baffelli (S'13) received the B.Sc. and M.Sc. degrees in electrical engineering from the Swiss Federal Institute of Technology, Zürich, Switzerland, in 2011 and 2013, respectively, and the Ph.D. degree (Dr. Sc.) from the same institution in 2019, with a dissertation on the calibration and applications of terrestrial radar interferometers.

His current research interests include the use of ground-based radar systems for the mapping of surface displacement, the analysis and correction of atmospheric phase screen in terrestrial differential interferometry, spatial statistics and the processing, calibration, and automatic of polarimetric terrestrial radar data.

Othmar Frey (S'04–M'08–SM'17) received the M.Sc. degree in geomatic engineering (hons.) from ETH Zurich, Zurich, Switzerland, in 2002, and the Ph.D. (Dr. Sc.Nat.) degree (hons.) in radar remote sensing from the University of Zurich, Zurich, Switzerland, in 2010.

He is a tenured Senior Researcher and Lecturer with ETH Zurich, Zurich, Switzerland, and also a Senior Scientist with GAMMA Remote Sensing AG, Gümligen, Switzerland. He has been working in this joint academic/industry setting since 2011. Previously, from 2002 to 2010, he was a Research Associate with the Remote Sensing Laboratories, University of Zurich. His research encompasses 2-D and 3-D (tomographic) synthetic aperture radar (SAR) focusing techniques and interferometric techniques for applications such as 3-D forest mapping, ground deformation monitoring (persistent scatterer interferometry / differential tomography), and profiling the structure of snowpacks, using spaceborne, airborne, and terrestrial radar sensors. He has been active in various national and international research projects, as a PI and project manager as well as a co-investigator. At GAMMA, he has also been active in the development of the Gamma Software and in technical consulting related to SAR imaging and interferometric applications.

Dr. Frey has been a member of the SAOCOM-CS Science Expert Group with the European Space Agency. Since 2015, he has been the Chair of the Swiss Chapter of the IEEE Geoscience and Remote Sensing Society. He was the recipient of the Distinction Award and Prize from the Faculty of Science, University of Zurich, for his Ph.D. dissertation, in 2010, and the ETH medal for an outstanding M.Sc. thesis, in 2002. He was the recipient of the 3rd Place Student Paper Award at the 2010 EUSAR Conference in Aachen, Germany, and he was a co-recipient of the Best Paper Award at the ISPRS Workshop Laserscanning and Silvilaser 2007 in Helsinki, Finland.

Irena Hajnsek (A'01–M'06–SM'09–F'14) received the Diploma degree (hons.) from the Free University of Berlin, Berlin, Germany, in 1996, and the doctorate degree (hons.) from the Friedrich Schiller University Jena, Jena, Germany, in 2001.

Since November 2009, she has been a Professor of Earth Observation with the Institute of Environmental Engineering, Swiss Federal Institute of Technology (ETH) Zurich, Zurich, Switzerland, and, at the same time, the Head of the Polarimetric SAR Interferometry Group, Microwaves and Radar Institute (HR), German Aerospace Center (DLR), Wessling, Germany. From 1996 to 1999, she was with the DLR-HR. From 1999 to 2000, she was with the Institut d'Electronique et de Telecommunications de Rennes, University of Rennes 1, Rennes, France, for ten months, in the frame of the EC-TMR Radar Polarimetry Network. In 2005, she was a Guest Scientist with the University of Adelaide, Adelaide, Australia, for six weeks. She is the Science Coordinator of the German Satellite Mission TanDEM-X. Her main research interests include electromagnetic propagation and scattering theory, radar polarimetry, SAR and interferometric SAR data processing techniques, and environmental parameter modeling and estimation.

Dr. Hajnsek was a member of the ESA Mission Advisory Group of the 7th Explorer Mission CoReH2O from 2009 to 2013. She was a Technical Program Co-Chair of the 2012 IEEE International Geoscience and Remote Sensing Symposium in Munich. Since 2013, she has been a member of the IEEE Geoscience and Remote Sensing Society Administrative Committee.